arXiv:2107.13589v1 [quant-ph] 28 Jul 2021

Improved quantum error correction using soft information

Christopher A. Pattison[1], Michael E. Beverland[2], Marcus P. da Silva[2], and Nicolas Delfosse[2]

[1]Caltech, Institute for Quantum Information and Matter, Pasadena, USA
[2]Microsoft Quantum and Microsoft Research, Redmond, USA

October 11, 2021

Abstract

The typical model for measurement noise in quantum error correction is to randomly flip the binary measurement outcome. In experiments, measurements yield much richer information—e.g., continuous current values, discrete photon counts—which is then mapped into binary outcomes by discarding some of this information. In this work, we consider methods to incorporate *all* of this richer information, typically called *soft information*, into the decoding of quantum error correction codes, and in particular the surface code. We describe how to modify both the Minimum Weight Perfect Matching and Union-Find decoders to leverage soft information, and demonstrate these soft decoders outperform the standard *(hard)* decoders that can only access the binary measurement outcomes. Moreover, we observe that the soft decoder achieves a threshold 25% higher than any hard decoder for phenomenological noise with Gaussian soft measurement outcomes. We also introduce a soft measurement error model with amplitude damping, in which measurement time leads to a trade-off between measurement resolution and additional disturbance of the qubits. Under this model we observe that the performance of the surface code is very sensitive to the choice of the measurement time—for a distance-19 surface code, a five-fold increase in measurement time can lead to a thousand-fold increase in logical error rate. Moreover, the measurement time that minimizes the physical error rate is distinct from the one that minimizes the logical performance, pointing to the benefits of jointly optimizing the physical and quantum error correction layers.

Due to the presence of errors and noise in quantum hardware, quantum error correction is essential for the scalability and usefulness of quantum computers [1]. The most promissing approaches to fault-tolerant quantum error correction revolve around the surface code [2, 3], which tolerates high error rates and is naturally implemented one a square grid of qubits using only local gates. Numerical simulations show that the surface code performs well for a variety of noise models [4], including gates corrupted by stochastic [3, 5] and coherent [6] errors. The error models that are typically considered include a very simple representation of noisy measurements where binary measurement outcomes during computations are flipped with some probability.

However, measurements in physical realizations of quantum computers are rarely, if ever, binary. Measurement outcomes are physically represented by much richer quantities, such as continuous currents or voltage, and are converted into binary outcomes by additional processing that discards some information. This is no different from the classical setting, where information is similarly represented by currents and voltages (including non-binary information, such as in the case of flash memories [7]). In classical error correction, this richer physical representation, often referred to as *soft information* (in contrast to the *hard* or *sharp* features of of binary information), is exploited to obtain greater tolerance to errors, or to reduce the noise required to achieve some logical error rate [8]. This naturally raises the question of how to extract similar benefits from soft information in the quantum setting. However, the classical approach of directly measuring the soft values of all bits and computing parities in noiseless post-processing cannot be applied to the quantum setting, as it would destroy the quantum superpositions being protected. Moreover, parities computed with quantum circuits

can propagate errors, since these quantum circuits are noisy. Fault-tolerant quantum error correction with soft information requires non-trivial modifications.

This challenge has been partially addressed in systems with continuous variable encodings of qubits [9–14]. Here we consider a more general setting, independent of the physical qubit encoding and grounded on the conditional distributions of the measurement outcomes. Our main result is the design of generic *soft decoders* for the surface code: a soft minimum weight perfect matching (MWPM) decoder (which we show identifies a most likely fault set for soft information), and a soft Union-Find (UF) decoder (which is an approximation to the MWPM decoder, but with comparable performance and low computational complexity). Both these decoders are modifications of existing surface code decoders [4, 15], with similar computational overhead, but may also be applied to other codes [16–20].

We evaluate the performance of these soft decoders numerically by introducing concrete measurement error models with soft information: one where the measurement outcome is correpted by white Gaussian noise (what we call *Gaussian soft noise*), and another where the measurement outcome is corrupted by amplitude damping and Gaussian noise (what we call *Gaussian soft noise with amplitude damping*). We observe several remakable properties of the soft UF decoder in the presence of soft Gaussian noise: the soft UF decoder outperforms the hard UF decoder (both in terms of threshold and peformance below threshold), and it also achieves a threshold that is 25% higher than the optimal threshold achievable by any hard decoder [21]. Moreover, we find that logical performance is highly sensitive to the measurement time. In the case of soft Gaussian noise with amplitude damping, minimizing physical measurement error rate can lead to logical error rates that are nearly 1000 times larger over what is achievable, despite such minimization leading to a measurement time that is only 5 times larger than the optimum.

We briefly review surface codes and provide some introductory definitions in Section 1. This section also describes our general framework to describe soft measurements, and gives specific examples including a model of the amplitude damping channel during measurement. In Section 2, we define a general noise model with soft measurement noise and we discuss the generalization of the traditional phenomenological model and circuit models. The soft MWPM decoder and the soft UF decoder are presented in Section 3. Then, we prove in Section 4 that the soft MWPM decoder returns a most likely fault set. We also provide a sufficient condition for the success of the soft UF decoder, proving that these two soft decoders perform well. In Section 5, we evaluate the performance of the soft UF decoder for the phenomenological model and the circuit model with soft noise. Finally, in Section 6, we use a toy model to illustrate the benefits of optimizing measurement with awareness of the fault-tolerant error correction protocol.

1 Background and definitions

1.1 Graph and hypergraphs

In this section, we review the language of graph and hypergraph theory [22].

A *graph* is a pair $G = (V, E)$ where V is the vertex set and E is the edge set. An edge $e \in E$ is a pair of vertices $e = \{u, v\}$. In this work, we consider only finite graphs. We will allow graphs to contain multiple copies of the same edge $\{u, v\}$.

To describe subsets of edges and vertices, it is convenient to introduce the language of chain complexes. A *1-chain* in a graph is defined to be a formal sum of edges $x = \sum_{e \in E} x_e e$ where $x_e \in \mathbb{Z}_2$. The 1-chain x can be interpreted as the subset of edges e such that $x_e = 1$. Conversely, any subset of E defines a 1-chain. Similarly, a *0-chain*, which represents a subset of V, is defined to be a formal sum of vertices $y = \sum_{v \in V} y_v v$ where $y_v \in \mathbb{Z}_2$. Given the correspondence between subsets and chains, we use the notation $e \in x$ (respectively $v \in y$) to refer to the fact that e (respectively v) belongs to the subset of edges corresponding to x (respectively y).

For $i = 0, 1$, the set of i-chains, denoted C_i, is a $\mathbb{Z}_2$-linear space equipped with the component-wise binary addition. The *boundary map* is a $\mathbb{Z}_2$-linear map ∂ from C_1 to C_0. The boundary of an edge $e = \{u, v\}$ is defined to be $\partial(e) = u + v$. and by linearity we have $\partial(x) = \sum_{e \in E} x_e \partial(e)$ for all $x \in C_1$. In other words, the boundary of a set of edges $A \subset E$ is the set of vertices that are incident with an odd number of edges of A. Note that if e_1 and e_2 are two edges in E which correspond to the same pair of vertices, we have that $\partial(e_1 + e_2) = 0$ by addition in $\mathbb{Z}_2$.

We also consider the restriction of the boundary to a subset of vertices. Given a subset $U \subset V$, the *restricted boundary map* $\partial_U : C_1 \to C_0$ is defined by

$\partial_U(x) = \sum_{v \in \partial(x) \cap U} v$.

In this work, we also consider finite hypergraphs. A *hypergraph* is defined as a pair $H = (V, E)$ where V is the vertex set and E is the set of hyperedges. The difference from a graph is that a hyperedge can be an arbitrary subset of V that may contain more than two vertices. Like in the case of graphs, a hypergraph can contain multiple copies of the same hyperedge. When the context is clear, we will often use the term edges to refer to the hyperedges of a hypergraph.

The chain complex language extends to hypergraphs. A 1-chain in a hypergraph is a formal sum of hyperedges and a 0-chain is a formal sum of vertices. The boundary of a hyperedge $e = \{v_1, \ldots, v_m\}$ is defined to be $\partial(e) = v_1 + \cdots + v_m$ and the boundary map is extended to all 1-chains by linearity as for graphs.

1.2 Surface codes

In this section, we briefly review[1] the implementation of quantum error correction with the surface code [25]. We focus on the rotated surface code represented in Figure 1(a). However, all the results of this article generalize immediately to any surface code with or without boundary, and also to hyperbolic surface codes [26].

The rotated surface code with minimum distance d encodes one logical qubit in a grid of $d \times d$ data qubits. Error correction with the surface code is based on so-called *plaquette measurements* which each return one outcome bit. Based on the outcomes extracted, a classical algorithm known as a decoder is used to identify errors which corrupt the data qubits.

A plaquette measurement is a weight-four Pauli measurement $X_a X_b X_c X_d$ or $Z_a Z_b Z_c Z_d$ acting on the four qubits a, b, c, d of a face of the grid of qubits. The boundary plaquettes represent weight-two measurements $X_e X_f$ or $Z_e Z_f$ acting on the two qubits of a face along the boundary of the grid.

A Pauli operator which is a product of plaquette operators is called a *stabilizer* of the surface code. This is because it acts trivially on encoded states. We sometimes refer to the measured plaquette operators as *stabilizer generators*.

By symmetry, X errors and Z errors can be corrected with the same strategy. In this section, we describe the correction of X errors based on the outcome of the measurement of Z plaquettes.

[1] Refs. [4, 23, 24] provide more complete overviews of quantum error correction and quantum computation with surface

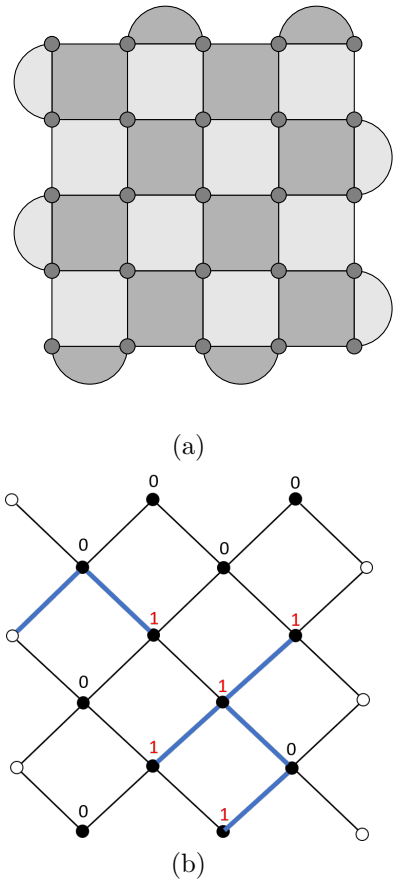


Figure 1: (a) The distance-five rotated surface code, which encodes one logical qubit into a grid of 5×5 data qubits (grey vertices). Blue and white plaquettes support Z and X measurements respectively. (b) A graphical representation of X errors in the distance-five surface code. Each of the 25 data qubits corresponds to an edge of the graph. Black vertices support Z plaquette measurements. White vertices are added to provide a second endpoint for edges associated with a qubit that is incident to a single Z measurement. During a stabilizer measurement round, each black vertex provides an outcome bit for a Z plaquette. The set of blue edges represents an X error, and the outcome in a black vertex is given by the parity of the number of incident blue edges.

First let's assume that there is some error on the qubits but that the plaquette measurements are performed perfectly. The value of the outcome bit returned by a plaquette measurement is then given by the parity of the number of qubits in the plaquette supporting the error. As a result, errors and measurement outcomes exhibit a natural graph structure as one can see in Figure 1(b). An X error, which is supported on the edges of the decoding graph G_X, can be represented by the 1-chain $x = \sum_{e \in E} x_e e$ such that $x_e = 1$ iff the edge e suffers from an X error. The set of outcomes produced by all the plaquette measurements is represented by a 0-chain $m = \sum_{v \in V} m_v v$ such that $m_v = 1$ iff the outcome bit returned in vertex v is non-trivial.

In practice, the measurement of a plaquette is not perfect. It is typically implemented using a small circuit that uses an additional ancilla qubit placed in the center of the plaquette. The ancilla qubit is prepared in an initial state $|0\rangle$ or $|+\rangle$ and a sequence of CNOT gates is performed between the ancilla qubit and the plaquette's qubits. Then, the outcome of the plaquette measurement is extracted by measuring the ancilla qubit in the Z or X basis. It is possible to simultaneously extract the outcome bit of all plaquettes in 6 time steps of operations by interleaving the CNOT gates in a particular order (see Section 2.4). We refer to the extraction of bits for the full set of a plaquettes of the surface code a *stabilizer measurement round*.

A single stabilizer measurement round is not enough to achieve good performance, because the measurement circuits are implemented with imperfect gates and the outcome measured is unreliable. To account for measurement errors, the standard solution is to perform error correction based on multiple consecutive rounds of measurement data, as we describe in more detail later.

1.3 Soft measurement

Measurements are subject to noise, as are other operations in quantum hardware. Three standard models of noise are typically considered in the field of quantum error correction. These all assume the depolarizing channel during operations on the qubits (including idling operations), but the models differ in how they treat plaquette measurements. The simplest is the *ideal measurement model* where plaquette measurements are assumed to be perfect. In the *phenomenological noise model*, this is amended by assuming that following each perfect plaquette measurement the binary outcome can be flipped before being reported. The *circuit noise model* is the most realistic of the standard models. In this case, plaquette measurements are implemented using explicit circuits built from more basic operations, including single-qubit measurements with a possible flip of the binary outcome.

In all three of these models, the outcomes of the stabilizer measurements are discrete, and therefore decoding algorithms are typically designed to operate using binary measurement outcomes. However, due to physical details of the measurement apparatus, the output from a physical system will not be a simple binary value, and may range from photon counts to continuous voltage waveform. This output may be processed into a binary outcome, but this processing may lead to information loss.

Here we seek to go beyond this paradigm. To do so, we introduce a simple model of measurement which produces a more general output; see Figure 2. More specifically, in our model of measurement there is first a projection of the state into a subspace $\pi_{\bar{\mu}}$ as in the standard models, but the *ideal outcome* $\bar{\mu} \in \{0, 1\}$ cannot be observed directly. What is observed is instead a *soft outcome* μ, whose distribution is given by the probability density function $f^{(\bar{\mu})}(\mu)$, which is conditioned on the ideal outcome $\bar{\mu} = 0$ or 1. Our formalism can easily handle both discrete and continuous measurement outcomes with minimal modifications. For brevity, we focus on continuous-valued soft measurement outcomes in this article.

Given the soft outcome, we can try to infer the ideal outcome by mapping the soft outcome onto a binary outcome that we refer to as the *hard outcome* $\hat{\mu}$. One particular choice for this *hardening map* corresponds to a maximum likelihood assignment, where

$$\hat{\mu} = \begin{cases} 0 & \text{if } f^{(0)}(\mu) \geq f^{(1)}(\mu), \\ 1 & \text{otherwise.} \end{cases} \tag{1}$$

We say that a *soft flip* occurs during a measurement if the hard outcome inferred is not equal to the ideal outcome. If the ideal outcome is $\bar{\mu}$, the probability of a soft flip is given by

$$\mathbb{P}(\text{soft flip}|\bar{\mu}) = \int_{f^{(\bar{\mu}')}(\mu) > f^{(\bar{\mu})}(\mu)} f^{(\bar{\mu})}(\mu) \mathrm{d}\mu, \tag{2}$$

where $\bar{\mu}' = \bar{\mu} + 1 \pmod 2$. In general, this probability depends on the value of the ideal outcome $\bar{\mu}$.

codes.

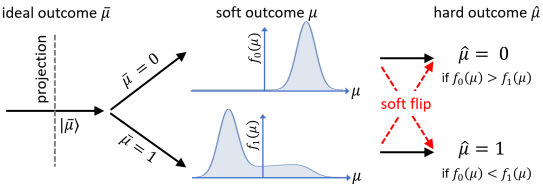


Figure 2: We model measurements as a perfect projection with ideal discrete outcome $\bar{\mu}$, followed by a noisy process which outputs a continuous soft outcome μ. The soft outcome can be processed to produce a discrete guess $\hat{\mu}$ of the ideal outcome, for example by comparing the probability density functions for μ conditioned on different cases of $\bar{\mu}$. There can be some loss of information in going from a soft to a hard outcome. When the hard outcome does not match the ideal outcome, we say a soft flip has occurred. Standard decoders use the hard outcome as their input, whereas we propose using the soft outcome directly for decoding.

We say that a measurement is *symmetric* if the probability of a soft flip is the same for both values of the ideal outcome $\bar{\mu} = 0$ or 1. We then define the probability $p_{M,\text{soft}} = \mathbb{P}(\text{soft flip}|0) = \mathbb{P}(\text{soft flip}|1)$ that a hard decoder interprets the soft outcome as a flip after hardening. In this work we often consider scenarios in which there can first be a flip of the ideal measurement outcome with probability p_M preceding symmetric soft noise. Then the probability $p_{M,\text{hardened}}$ of a flip overall after hardening is

$$p_{M,\text{hardened}} = p_M + p_{M,\text{soft}} - p_M p_{M,\text{soft}}. \quad (3)$$

A simple example of a symmetric soft measurement is the *Gaussian soft noise* in which a $f^{(0)} = \mathcal{N}(+1, \sigma^2)$ and $f^{(1)} = \mathcal{N}(-1, \sigma^2)$. Some physical processes may lead to asymmetric measurements, as we discuss next in Section 1.4.

1.4 Example: Amplitude damping

Here we provide a toy model [27] for soft measurement noise based on *amplitude damping* [28] which is common in solid state quantum devices such as superconducting qubits and quantum dots [29, 30]—we call this model *Gaussian soft noise with amplitude damping*. In this case the probability density functions $f^{(0)}$ and $f^{(1)}$ can be tuned by setting the relative duration of three timescales τ_M, τ_A and τ_F; see Figure 3. We therefore write these as $f^{(0)}(\mu; \tau_M, \tau_\text{A}, \tau_F)$ and $f^{(1)}(\mu; \tau_M, \tau_\text{A}, \tau_F)$, making their dependence on $\tau_M, \tau_\text{A}, \tau_F$ explicit.

Under this noise model, at any infinitesimal time interval the qubit may decay from $|1\rangle$ to $|0\rangle$ with a fixed time-independent rate $1/\tau_\text{A}$, but no transitions from $|0\rangle$ can occur. Here we refer to τ_A as the *amplitude damping time*, although in the physics literature it is often referred to as the T_1 time. This asymmetry arises because in many systems the $|1\rangle$ state has higher energy than the $|0\rangle$ state, and unintentional interactions with a low-temperature bath lead to energy transfer from the qubit to the bath, resulting in this decay (for this reason, amplitude damping is also known as *energy relaxation*).

Since measurement relies on the accumulation of information about the state over the *measurement time* τ_M, any qubit decays during that time will increase the probability that a $|1\rangle$ at the beginning of the measurement is mistaken for a $|0\rangle$, but not the other way around.

In our amplitude damping model model, there is a signal $S(t)$ which builds up over time t starting from $S(0) = 0$. The signal's behavior is mathematically equivalent to a one-dimensional continuous random walk with drift, where the sign of the drift depends on whether the system is in the state $|0\rangle$ or $|1\rangle$. Specifically, if the state of the system is $|0\rangle$ during an infinitesimal time interval from t to $t + \mathrm{d}t$, the mean of S is increased by an amount proportional to $\mathrm{d}t$. On the other hand if the state of the system is $|1\rangle$ during this interval, the mean of S is decreased by the same amount. Irrespective of the state of the system, the variance of S increases by an amount proportional to $\mathrm{d}t$ during this time interval. The ratio between the variance and the square of the mean of the increment over a small time interval is $\tau_F/\mathrm{d}t$, where the constant τ_F is refered to as *the fluctuation time*. The signal is read out at a time τ_M giving $S(\tau_M)$ which we take to be the continuous measurement outcome μ (after scaling such that the mean of μ is $+1$ when $\bar{\mu} = 0$).

Although the derivation and precise forms of the conditional distributions under this toy model are somewhat involved (see Appendix A), their qualitative behavior is rather simple, as illustrated by Figure 3. When $\tau_M \ll \tau_\text{A}$, the distributions are well approximated by Gaussians. These Gaussians have an overlap that decreases monotonically with τ_M/τ_F, so and increasing τ_M/τ_F lowers $\mathbb{P}(\text{soft flip}|\bar{\mu})$. As τ_M approaches τ_A, $f^{(0)}$ remains unchanged but $f^{(1)}$ is distorted and shifts towards $f^{(0)}$, so that as $\frac{\tau_M}{\tau_\text{A}}$ increases $\mathbb{P}(\text{soft flip}|1)$ approaches $\frac{1}{2}$ (the distributions overlap completely). A regime of particular interest

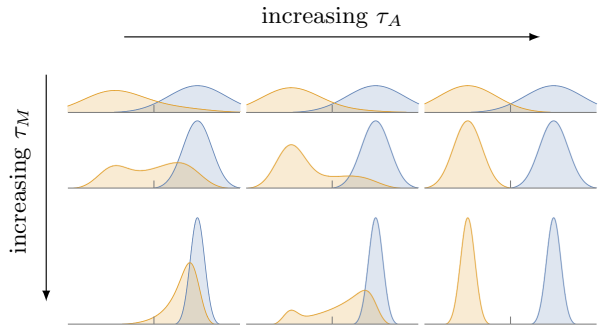


Figure 3: Conditional probability density functions $f^{(0)}$ (blue) and $f^{(1)}$ (yellow) for τ_M/τ_F increasing from top to bottom, and τ_A/τ_F increasing from left to right. The width of $f^{(0)}$ is proportional to $\sqrt{\tau_F/\tau_M}$, and the scales are chosen so that for $\tau_M \ll \tau_A$ the Gaussians are centered at ± 1. Intuitively, increasing measurement time τ_M narrows the conditional distributions (making them more distinguishable), while decreasing amplitude damping lifetime τ_A shifts the $\bar{\mu} = 1$ distribution towards the $\bar{\mu} = 0$ distribution (making them less distinguishable).

in this model is when $\tau_F \ll \tau_M \ll \tau_A$, so that $f^{(1)}$ is not significantly distorted ($\tau_M \ll \tau_A$), while the overlap between the conditional distributions is also small ($\tau_F \ll \tau_M$).

2 Graphical models for soft noise in the surface code

In this section, we propose a general graphical noise model to describe errors and soft measurement outcomes for surface codes, including correlated errors and repeated measurements. This formalism includes the standard noise models mentioned in Section 1.2 namely ideal measurement noise, phenomenological noise and circuit noise [4] as special cases. Later in Section 3 we define decoders which correct the errors in graphical noise models, and in particular which make use of the soft data to outperform standard decoders which ignore this soft information.

2.1 General graphical model

Here we present a general graphical model for arbitrary Pauli noise with soft measurement outcomes. Faults can affect the outcomes of plaquette measurements of the surface code and can leave residual errors on the data qubits. The following definition captures this notion.

Definition 2.1. *A* graphical model *for T rounds of measurements with the surface code is a quadruple (G_T, p, f, π) defined by*

- **Fault hypergraph:** *A hypergraph $G_T = (V_T, E_T)$ such that V_T contains a vertex (a, t) for each plaquette a and for each round $t = 1, \ldots, T$.*
- **Fault probability:** *A value $p_e \in [0, 1]$ for each hyperedge $e \in E_T$.*
- **Measurement noise:** *A pair of probability density functions $(f^{(0)}_{a,t}, f^{(1)}_{a,t})$ for each plaquette a and for each round $t = 1, \ldots, T$ describing the measurement outcome in this location.*
- **Residual error:** *A Pauli error π_e on the data qubits of the surface code for each hyperedge $e \in E_T$.*

We call the graph G_T the *fault hypergraph* or simply fault graph when it is a proper graph. To construct the graph G_T in this case, we begin by including all the vertices from G_X and G_Z described in Section 1.2 for each of the $T + 1$ layers. The set of *measurement vertices* of G_T, denoted $V_\bullet$, is the set of vertices (a, t) corresponding to the spacetime locations of the plaquettes, where a corresponds to the plaquette and t labels the measurement round. Each hyperedge of G_T represents a potential fault and the vertices contained in a hyperedge correspond to the spacetime locations of measurements that detect this fault. In practice, a fault may correspond to a Pauli error X, Y or Z or the flip of an outcome bit. It could also be a combination of multiple Pauli errors and outcome bit flips. The fault e induces a *residual error* π_e on the data qubits at the end of the T rounds of measurement. The hypergraph G_T may contain multiple copies of the same edge e with different residual errors π_e. The graph G_T contains additional vertices which we call *boundary vertices*, denoted $V_\circ = V \backslash V_\bullet$. Figure 4 shows an example of a graphical noise model which corresponds to $T = 3$ rounds of measurement for the distance $d = 5$ surface code.

In some cases, it is useful to define independent noise models for X type errors and Z type errors in which case we define a separate hypergraph for each. The X-type hypergraph contains vertices (a, t) for Z plaquettes only.

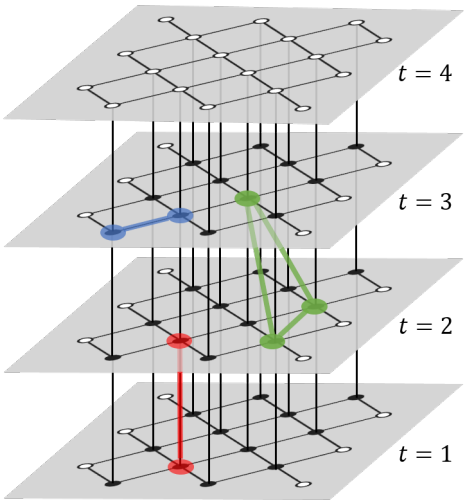


Figure 4: Examples of hyperedges corresponding to faults. A single-qubit X error corresponds to a singe horizontal edge (blue). A flipped measurement outcome corresponds to a singe vertical edge (red). More general faults are possible, and correspond to hyperedges. Here we show an example of a weight-two Pauli error and the resulting syndrome that could arise from a single fault in a stabilizer measurement circuit (green).

2.2 Sampling from graphical models

In our graphical noise models, faults occurs independently of one another. Correlated errors acting on different qubits at potentially different times can occur since each fault has no restriction on the support of the residual error or on the measurement vertices which it flips.

A *fault set* for the graphical model G_T is defined to be a 1-chain x of G_T, that is a formal sum of hyperedges $x = \sum_{e \in E_T} x_e e$. The *probability of a fault set* x is

$$\mathbb{P}(x) = \prod_{e \in x} p_e \prod_{e \notin x} (1 - p_e), \tag{4}$$

where each fault e occurs with probability p_e.

For a trivial fault set, $x = 0$, the *ideal outcome* in any measurement vertex (a, t) is $\overline{m}_{a,t} = 0$. A fault e, containing a measurement vertex (a, t), induces a change of the value of the ideal outcome $\overline{m}_{a,t'}$ for all $t' \geq t$. The ideal outcome associated with a general fault set x is obtained by combining the effects of all its faults $e \in x$.

The soft outcome $m_{a,t}$ and the hard outcome $\hat{m}_{a,t}$ are generated from the ideal outcome using the probability density functions $f^{(0)}_{a,t}$ and $f^{(1)}_{a,t}$ as explained in Section 1.3. Note that although we use the term 'ideal outcome', this outcome depends on faults that have occurred at earlier times.

For the decoders we define later it is also convenient to introduce the syndrome which measures the changes between two consecutive rounds of measurements. The *syndrome*, denoted $\hat{s}(m)$, is a 0-chain in G_T which can be calculated from the observed soft measurement outcomes m by first using Eq. (1) to identify the hard outcomes $\hat{m}$, and then

$$\hat{s}_{a,t} = \hat{m}_{a,t} + \hat{m}_{a,t-1} \pmod 2 \tag{5}$$

for all measurement vertices (a, t), with the convention $\hat{m}_{a,0} = 0$. The value of the syndrome in boundary vertices is 0. The syndrome provides the same information as the hard outcome but it is more convenient for the decoder to use the syndrome as an input instead of the hard outcome.

2.3 Example: Soft phenomenological noise

Here we define a generalization of the standard phenomenological noise model introduced in [4] to include soft Gaussian noise affecting measurement outcomes.

First we define the noise model's X-type *fault graph* G_T, by stacking $T + 1$ copies of the graph G_X which was described in Section 1.2 and represented in Figure 1(b), and connecting consecutive layers with vertical edges; see Figure 5. The graph G_T has two types of vertices. Specifically, the set of *measurement vertices* of G_T, denoted $V_\bullet$, is the set of vertices (a, t) corresponding to the space time locations of the plaquettes, where a corresponds to a plaquette and $t = 1, \ldots, T$ labels the measurement round. The remaining vertices are *boundary vertices*, denoted $V_\circ = V \backslash V_\bullet$. The vertices of the $T + 1$ layer are treated differently from other vertices in G_T, in that they correspond to perfect measurements.

Furthermore, a probability p_D is assigned to each horizontal edge, and a probability p_M is assigned to each vertical edge in G_T. This corresponds to qubits being affected by independent X errors with probability p_D and independent ideal measurement outcome flips with probability p_M. The pair of probability density functions $f^{(0)}$ and $f^{(1)}$ are assigned to each measurement vertex in G_T.

In this graphical description of the noise model, edges represent potential faults and the vertices contained in an edge correspond to the measurements

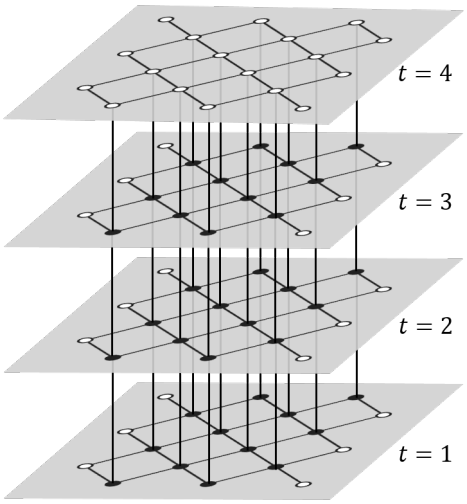


Figure 5: Fault graph for the soft phenomenological noise model with $T = 3$ rounds of measurements for the surface code with distance five. The graph contains $T + 1 = 4$ copies of the graph represented in Figure 1(b). There is a copy of the graph for each time step and an additional copy corresponding to a round of perfect measurement is added for a proper termination. Horizontal edges correspond to qubit errors and vertical edges encode ideal outcome flips.

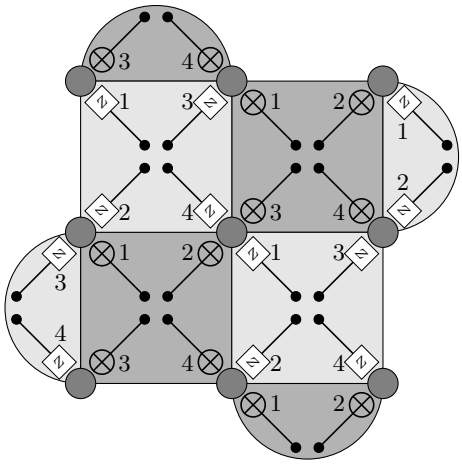


Figure 6: Standard stabilizer extraction circuit for a distance 3 rotated surface code (see for instance [31]). The circuit for an arbitrary distance code is obtained by translating this circuit for all stabilizers. Note that there are some idle circuit locations during which CNOT gates are being applied and others during which measurement qubits are being applied, which we treat separately in our model since measurement and gate times can be different.

whose ideal value will *change* due to the presence of this fault. For instance, the fault corresponding to the horizontal edge $\{(a,t),(b,t)\}$ in G_T is an X error being applied just before round t of measurements to the qubit associated with the edge (a,b) in G_X. This fault occurs with the probability assigned to the edge, namely p_D, and it results in a change of the ideal outcome associated with the plaquettes a and b at time t. In other words, it results in a change of the ideal outcomes of vertices (a,t) and (b,t) when compared with $(a,t-1)$ and $(b,t-1)$ respectively. In the absence of additional faults, these vertices then retain their new ideal outcome for all rounds $t' \geq t$. The fault corresponding to the vertical edge $\{(a,t),(b,t+1)\}$ in G_T is a flip of the ideal outcome of the plaquette associated with a in G_X only at round t. This fault occurs with probability p_M, and corresponds to a change in the ideal outcome of the vertex (a,t) with respect to the vertex $(a,t-1)$ and then a further change of the ideal outcome of the vertex $(a,t+1)$ with respect to the vertex (a,t).

If the ideal outcomes were reported, this would precisely reproduce the standard phenomenological noise model introduced in Ref. [4]. Instead, the reported output of each plaquette in each round is the soft outcome obtained by sampling from the probability density functions assigned to the vertices of G_T, namely $f^{(0)}$ for plaquettes with ideal outcome 0 and $f^{(1)}$ for plaquettes with ideal outcome 1.

2.4 Example: Soft circuit noise

Here we provide a generalization of the standard circuit noise model to include soft measurement. Our model involves T consecutive stabilizer measurement rounds, where each measurement round is implemented by the circuit shown in Figure 6.

Each of the components of the circuit can fail in specific ways, and for each of these possible failures we introduce a hyperedge to the graph G_T. In particular, the following failures can occur for the circuit components:

- Idle qubits waiting for CNOT gates: X, Y, Z each occurs independently with probability $p_{IG}/3$.
- Idle qubits waiting for measurements: X, Y, Z each occurs independently with probability $p_{IM}/3$.
- CNOT gates: XI, YI, ZI, IX, XX, YX, ZX, IY, XY, YY, ZY, IZ, XZ, YZ, ZZ each occurs independently with probability $p_{\mathrm{CNOT}}/15$.

- Measurement outcomes (ideal): have their ideal outcome flipped with probability p_M.
- Measurement outcomes (soft): given the ideal outcome $\bar{\mu} \in \{0, 1\}$, the continuous outcome μ is sampled from the probability density function $f^{(\bar{\mu})}(\mu)$ as described in Section 1.3.

A few remarks are called for before describing how the graphical noise model is constructed. First note that the circuit in Figure 6 only has time steps during which either CNOTs or measurements are performed (but not both), making it natural to consider the two above scenarios for idle qubits since a CNOT gate may have a very different duration than a measurement. Secondly, here each fault (even faults associated with the same operation in the circuit) are applied independently. At first this may seem slightly different from the standard circuit noise considered in the literature in different faults that occur on the same operation are exclusive. However, the standard exclusive circuit noise model and the inclusive circuit noise model assumed here are actually exactly equivalent as proven in Appendix E of [18]. When mapping between the inclusive and exclusive noise models, the probability with which each fault occurs can change, although the change is very small in the regimes of interest. We discuss this in more detail in Appendix B.

To construct the graph G_T in this case, we begin by including all the vertices from G_X and G_Z for $T + 1$ layers from Section 1.2. For each of the possible faults listed in the first four bullet points (i.e. excluding the soft measurement) that can occur in the T rounds of stabilizer measurements implemented by the circuit, a hyperedge is added to the graph G_T. The vertices included in the hyperedge are those vertices whose measurement outcomes will flip if that fault occurs. The probability assigned to the hyperedge is simply the probability that the fault occurs. The residual error associated with the hyperedge is identified by observing what Pauli operator is left on the data qubits at the end of the measurement round during which the fault occurs. Lastly, each measurement vertex has the pair $\{f^{(0)}(\mu), f^{(1)}(\mu)\}$ of probability density functions assigned.

3 Soft decoding

In this section, we propose two efficient decoders for surface codes with soft measurements. First, we propose a soft version of the minimum weight perfect matching (MWPM) decoder [4]. Different variants of the MWPM decoder exploiting some soft information were considered previously for the special case of GKP surface codes [11–14]. Although its complexity is polynomial, the soft MWPM decoder may be too slow for some applications. Next, we propose a soft version of the Union-Find (UF) decoder [15] which has lower complexity and therefore could be more practical.

3.1 Decodability constraints

The ultimate goal of a decoder is to correct the data qubits, that is to cancel the effect of the residual errors of the faults which occur. The two decoders proposed in this article return a fault set x for a given set of soft outcomes. The correction to apply to the data qubits is the product of the residual errors π_e corresponding to the faults e in x.

We will restrict ourselves to graphical models (G_T, p, f, π) that satisfy the following *decodability conditions*:

(C1) All the edges in G_T have rank two.

(C2) For all $e \in E_T$, we have $p_e < 0.5$.

Condition (C1) guarantees that G_T is a graph instead of a general hypergraph. We require this because we expect the decoding problem for a general hypergraph to be too difficult to solve. For example, the problem of identifying a least likely fault set in that case includes the three-dimensional matching problem which is NP-hard [32]. Condition (C2) excludes pathological cases where faults occur with excessively high probability.

3.2 Soft decoding graph

In Section 2.1 we defined the fault hypergraph. Here, we introduce another graph which will be used for decoding. The *decoding graph*, denoted $\tilde{G}_T = (\tilde{V}_T, \tilde{E}_T)$, associated with the graphical model (G_T, q, f, π) is the graph obtained from G_T by adding an edge (which we call a soft vertical edge) connecting (a, t) with $(a, t + 1)$ when (a, t) is a measurement vertex. The graph G_T may already contain a vertical edge connecting these two vertices. In that case, the decoding graph $\tilde{G}_T$ contains two edges connecting (a, t) and $(a, t + 1)$ that we refer to as the soft vertical edge and the hard vertical edge. Moreover, all the boundary vertices of $\tilde{G}_T$ are identified to single vertex, denoted v_g, that we refer to as the *ghost vertex*.

By definition, we have $\tilde{V}_T = V_\bullet \cup \{v_g\}$ and $\tilde{E}_T$ is the set E_T augmented with soft vertical edges.

Consider a measurement vertex (a,t). let μ be the soft outcome observed in this vertex and $\hat{\mu}$ be the corresponding hard outcome. Denote by $\hat{\mu}' = \hat{\mu} + 1 \pmod 2$ the other value of the hard outcome. To define edge weights in the decoding graph, it is convenient to introduce the *likelihood ratio*

$$L_{a,t}(\mu) = \frac{f_{a,t}^{(\hat{\mu}')}(\mu)}{f_{a,t}^{(\hat{\mu})}(\mu)}. \tag{6}$$

This ratio can be computed from the knowledge of the probability density functions and the value of the soft outcome μ because $\hat{\mu}$ and $\hat{\mu}'$ are derived from μ. By definition of the hard outcome, we have $L_{a,t}(\mu) \in [0,1]$.

Given the model parameters p_e and the set of soft outcomes m observed over measurement vertices, we define edge weights for the decoding graph. Hard and soft edges have different weights. The weight of the soft edge e between (a,t) and $(a,t+1)$ is defined as a function of the soft outcome, whereas the hard edge weight depends on the parameter p_e. Precisely, the edge weight is defined by

$$w(e) = \begin{cases} -\log L_{a,t}(m_{a,t}) & \text{if } e \text{ is soft,} \\ -\log\big(p_e/(1-p_e)\big) & \text{otherwise.} \end{cases} \tag{7}$$

These edge weights are non-negative numbers. In some cases, we denote this weight by $w_{\tilde{G}_T}(e)$ to avoid any ambiguity about which graph the weight is defined with respect to.

3.3 Soft Minimum Weight Perfect Matching decoder

Our soft MWPM decoder is specified in Algorithm 1. The key ingredient is the distance graph that we introduce below.

We consider the distance in the decoding graph $\tilde{G}_T$ induced by the edge weights $w_{\tilde{G}_T}(e)$. The length of a path in $\tilde{G}_T$ is defined to be the sum of the weights of its edges. The *distance* between two vertices u and v, denoted $d_{\tilde{G}_T}(u,v)$, is defined to be the minimum length of a path connecting u and v. A minimum length path joining u and v is called a *geodesic*. Given $u, v \in V_T$, let $\mathrm{geo}(u,v)$ be the set of edges supporting a geodesic connecting u and v. If the decoding graph contains multiple geodesics between u and v, $\mathrm{geo}(u,v)$ is chosen arbitrarily among them. We will consider $\mathrm{geo}(u,v)$ as a 1-chain in the decoding graph.

Algorithm 1 Soft MWPM decoder

Input: The decoding graph $\tilde{G}_T$ for T rounds of measurements. A set of soft outcomes m.

Output: A fault set, *i.e.* a 1-chain x in G_T.

1: For each soft vertical edge e, compute $w_{\tilde{G}_T}(e)$ as a function of m using Eq. (7).
2: Compute the syndrome $\hat{s}$ from m using Eq. (5). Let $v_1, \ldots, v_k$ be the set of vertices of $\tilde{G}_T$ with non-trivial syndrome.
3: Construct the distance graph $K(\hat{s})$ with vertex set $V_K = \{v_1, \ldots, v_k\}$ and compute the edge weights $w_K(\{v_i, v_j\}) = d_{\tilde{G}_T}(v_i, v_j)$ using Dijkstra's algorithm.
4: Compute a minimum weight perfect matching M in $K(\hat{s})$.
5: For each edge $\{u,v\} \in M$, compute a geodesic $\mathrm{geo}(u,v)$ in the graph $\tilde{G}_T$.
6: **return** the 1-chain $\tilde{x} = \sum_{\{u,v\}\in M} \mathrm{geo}(u,v)$ restricted to the graph G_T.

Given the decoding graph $\tilde{G}_T$ and a syndrome $\hat{s}$, the *distance graph* $K(\hat{s}) = (V_K, E_K)$ is defined to be the fully connected graph with vertex set V_K given by the set of measurement vertices supporting a non-trivial syndrome. If $K(\hat{s})$ contains an odd number of vertices, we add the ghost vertex to V_K. We define edge weights in K based on the distance in the decoding graph, that is $w_K(\{u,v\}) = d_{\tilde{G}_T}(u,v)$.

Like in the standard MWPM decoder, the basic idea of Algorithm 1 is to compute a minimum set of paths that connect pairs of syndrome vertices in the decoding graph. This is done using a Minimum Weight Perfect Matching (MWPM) algorithm [33]. The distance graph contains an even number of vertices and its edge weights are non-negative making the application of the MWPM algorithm straightforward.

The main difference between our soft MWPM decoder and the standard hard MWPM decoder [4] is that the weights in the soft decoding graph depend on the set of outcomes m whereas they are fixed in the hard case. As a result, the distances between all pairs of nodes can be precomputed in the standard MWPM but not in the soft MWPM decoder. Similarly, one cannot precompute a geodesic for each pair of nodes in the soft decoding graph. This increases the execution time of the decoder. However, as we explain below, the worst-case asymptotic complexity is no worse than the standard MWPM decoder.

The worst case complexity of the standard MWPM

decoder is dominated by the call of the MWPM algorithm. Based on Blossom V, a popular implementation of a MWPM algorithm designed by Kolmogorov [34] which has a worst case complexity in $O(n_v^3 n_e)$ for a graph with n_v vertices and n_e edges, one can achieve a worst case complexity in $O(|V_T|^5)$ for the hard MWPM decoder, that is $O(d^{15})$ if $T = d$ rounds of measurement are used. Other implementations of the MWPM decoder achieve a better worst-case complexity but they might not run faster in practice (see Table I in [35]). The most favorable asymptotic scaling for a MWPM algorithm [36] leads a worst-case complexity in $O(\sqrt{n_v} n_e)$ for the matching subroutine and a MWPM decoder complexity in $O(d^{7.5})$ for $T = d$.

If Blossom V is used, the complexity of our soft variant of the MWPM decoder remains the same, $O(d^{15})$, dominated by the cost of this MWPM subroutine. We can also achieve $O(d^{7.5})$ worst-case complexity using the MWPM algorithm of [36] despite the fact that distances and geodesic between the syndrome nodes must be computed on the fly in our soft MWPM decoder. The computation of all the distances $d_{\tilde{G}_T}(v_i, v_j)$ is performed in step 3 and 4 of the algorithm with worst-case complexity $O(|V_T||E_T| + |V_T|^2 \log |V_T|)$ using Dijkstra's algorithm. Assuming $T = d$ measurement rounds, this subroutine runs in $O(d^6 \log d)$. The geodesics are computed in step 7 of Algorithm 1 also thanks to Dijkstra's algorithm with the same worst-case complexity as the distances calculation.

3.4 Soft Union-Find decoder

Here we provide a soft version of the UF decoder [15, 37], which achieves an error correction performance similar to the MWPM decoder but with better time complexity. Our soft UF decoder is specified in Algorithm 2.

The soft UF decoder works in two steps: First, we grow clusters of qubits in the decoding graph until each of the clusters can be corrected separately. The growth subroutine is shown in Figure 7. Then, the peeling decoder [38] is used to find a correction inside the grown clusters in linear time. In what follows, we explain the growth procedure used in our soft UF decoder.

To describe our soft UF decoder, it is convenient to introduce the *split-edge* graph $\tilde{H}_T$ obtained from the decoding graph $\tilde{G}_T$ by adding a vertex in the middle of each edge. Each edge e of the decoding

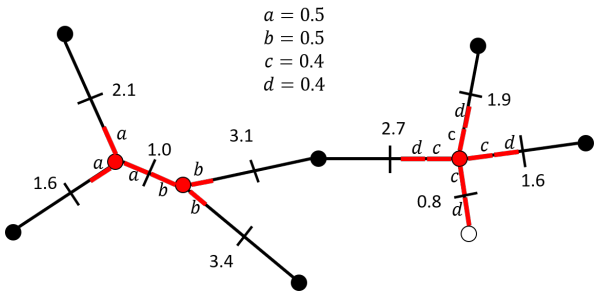


Figure 7: Illustration of the cluster growth subroutine of the UF decoder. Edges of the decoding graph are split in the middle. The three red vertices support a non-trivial syndrome. Initially, there are three odd clusters, one for each syndrome vertex. One odd cluster has perimeter four and the other two have perimeter three. At the first growth step, we select a cluster with minimum perimeter and we grow the three edges (a) by 0.5. Then, the edges (b), which belong to the least recently grown cluster with perimeter three, are grown. This connects two odd clusters forming an even cluster. During the next two steps ((c) and (d)), the remaining odd cluster grows until it meets a boundary node and becomes even.

graph splits into two edges of $\tilde{H}_T$ whose weights are given by $w_{\tilde{G}_T}(e)/2$. The boundary vertices of $\tilde{H}_T$ are those corresponding to boundary vertices of $\tilde{G}_T$.

To keep track of the edge growth, we associate a *growth state* $\gamma(e) \in \mathbb{R}$ with each edge e of $\tilde{H}_T$. An edge e is said to be *fully grown* if $\gamma(e) = w_{\tilde{H}_T}(e)$. The *cluster* of a vertex v of $\tilde{H}_T$ is defined to be the set of vertices of $\tilde{H}_T$ that can be reached from v through a path of fully grown edges.

Given a syndrome $\hat{s}$, a cluster of $\tilde{H}_T$ is said to be *even* if it contains an even number of vertices of $\hat{s}$ or at least one boundary vertex. A cluster that is not even is said to be *odd*. If a cluster is even, we can use the peeling decoder to determine a fault set included in the cluster which cancels the syndrome of this cluster [38]. Therefore, we will grow odd clusters until all clusters are even and can be corrected by peeling.

To determine which cluster to grow first, we consider the set $B(C)$ of edges of $\tilde{H}_T$ connecting a cluster C and its complementary. The *perimeter* of the cluster C is defined as the number of edges in $B(C)$. At the beginning of the growth procedure, the growth state of each edge is initialized to $\gamma(e) = 0$. Then, at each growth step, we select an odd cluster C with minimum perimeter and grow all edges of $B(C)$ by

incrementing the growth states by

$$\Gamma_C = \min_{e \in B(C)} (w_{\tilde{H}_T}(e) - \gamma(e)). \tag{8}$$

Γ_C is the smallest value Γ such that growing all edges of $B(C)$ by Γ fills at least one edge. If multiple odd clusters have the same perimeter, we prioritize the least recently grown cluster.

After the growth, we are left with only even clusters, and we will call the peeling decoder to find an estimation of the fault set inside the grown clusters. We consider the set $\varepsilon \subset \tilde{E}_T$ of edges of the decoding graph $\tilde{G}_T$ for which both halves are fully grown in the split-edge graph $\tilde{H}_T$. The peeling decoder takes as input the subset $\varepsilon \subset \tilde{E}_T$ and a syndrome $\hat{s}$ and computes, in linear time, a 1-chain $\tilde{x} \subset \varepsilon$ in $\tilde{G}_T$ such that $\partial_{V_\bullet}(\tilde{x}) = \hat{s}$. We will use the notation $\tilde{x} = \textbf{Peeling}(\varepsilon, \hat{s})$. The restriction of $\tilde{x}$ to G_T is the output the soft UF decoder.

Algorithm 2 Soft UF decoder

Input: The graph $\tilde{H}_T$ for T rounds of measurements. A set of soft outcomes m.
Output: A 1-chain x in G_T.

1: For each soft vertical edge e, compute $w_{\tilde{H}_T}(e)$ as a function of m using Eq. (7).
2: Compute the syndrome $\hat{s}$ from m using Eq. (5).
3: For each edge e of $\tilde{H}_T$, set $\gamma(e) = 0$.
4: While there exists at least one odd cluster do:
5: Select an odd cluster C with minimum perimeter. If there are multiple such clusters select the least recently grown.
6: Compute Γ_C defined in Eq. (8).
7: For all $e \in B(C)$ do $\gamma(e) \leftarrow \gamma(e) + \Gamma_C$.
8: Compute the set ε of edges e of $\tilde{G}_T$ such that the two halves of e in $\tilde{H}_T$ are fully grown.
9: Compute the 1-chain $\tilde{x} = \textbf{Peeling}(\varepsilon, \hat{s})$ of $\tilde{G}_T$.
10: **return** the restriction of $\tilde{x}$ to the graph G_T.

The growth procedure of our soft UF decoder Algorithm 2 differs from the growth of the variant of the UF decoder proposed in [37] in two ways. First, we grow half-edges instead of the original edges of the decoding graph. This is why we perform the growth in the graph $\tilde{H}_T$ instead of $\tilde{G}_T$. Second, we prioritize the least recently grown cluster. We checked that these two modifications bring a small improvement of the error threshold of hard UF decoder for the standard circuit noise model.

The time complexity of the soft UF decoder depends on the precision required for the edge weights of the soft decoding graph. Like in the circuit level study of [37], we expect that a finite precision is sufficient to achieve good decoding performance. Our simulations are done with 32-bits of precision for the edge weights. In that case, the worst case complexity of the soft UF decoder remains $O(d^3\alpha(d))$, where $\alpha(d)$ is the slowly increasing inverse Ackermann function. This complexity is significantly better than the soft MWPM decoder.

4 Proof of decoding success

In this section, we prove that the soft MWPM decoder and the soft UF decoder perform well. First, we prove that the soft MWPM decoder returns a most likely fault set. A key technical ingredient to establish this result is Lemma 4.3 which provides the probability of a fault set given a set of soft outcomes as a function of the edge weights in the soft decoding graph. Then, we propose a sufficient condition for the success of the soft UF decoder.

4.1 Technical definitions

Here we provide some definitions which are useful throughout this section.

Given a weighted graph G and a 1-chain a, we denote by $|a|_w = \sum_{e \in a} w(e)$ the sum of the edge weights in a. The diameter of a subset C of vertices of the graph, denoted $\text{diam}_w(C)$, is the maximum distance between two vertices of C assuming that edge lengths are given by $w(e)$. The diameter of a subset of edges or a 1-chain is defined to be the diameter of the set of incident vertices.

A fault set for a graphical model is a 1-chain in the fault graph G_T. Similarly, we can represent the set of soft flips for a given fault set x with a set of soft outcomes m as a 1-chain x_{soft} in the graph $\tilde{G}_T$ with support on soft vertical edges. In what follows, we denote $\tilde{x} = x + x_{\text{soft}}$ the 1-chain representing a fault set and its soft flips for a given set of soft outcomes. The value of x_{soft} depends on x and the set of soft outcomes observed m.

The syndrome $\hat{s}(m)$ can be derived from the value of $\tilde{x}$ because $\hat{m}$ can be computed from x and from the location of the soft flips. As a result, we can talk about a fault set $\tilde{x}$ with trivial syndrome.

The *weighted minimum distance* of a graphical model, denoted d_w, is defined to be the minimum value $|x|_w$ for a fault set x such that the residual error is a non-trivial logical error of the surface code.

To guarantee that the soft UF decoder performs well, we assume that the graphical model satisfies the following topological property.

(C3) Let $\tilde{x}$ be a fault set with trivial syndrome. If the diameter of $\tilde{x}$ satisfies $\mathrm{diam}_w(\tilde{x}) < d_w$ then $\pi(x)$ is a stabilizer of the surface code.

Both soft circuit noise and soft phenomenological noise satisfy this condition with Gaussian soft measurements and amplitude damping soft measurements, which include the cases we study numerically.

4.2 Success of the soft MWPM decoder

The goal of this section is to prove the following result.

Theorem 4.1. *For any graphical model satisfying (C1) and (C2), the soft MWPM decoder (Algorithm 1) returns a most likely fault set.*

Proof. Let m be a set of soft outcomes for a graphical model (G_T, p, f) and let $\hat{s}$ be the corresponding syndrome. Given m as an input, Algorithm 1 first generates the distance graph $K(\hat{s}) = (V_K, E_K)$ associated with $\hat{s}$. Then, it computes a minimum weight matching $M \subseteq E_K$ and the corresponding 1-chain

$$\tilde{x}_M = \sum_{\{u,v\} \in M} \mathrm{geo}(u, v)$$

in the decoding graph $\tilde{G}_T$. The output of Algorithm 1 is the fault set x_M which is the restriction of $\tilde{x}_M$ to G_T. We will prove by contradiction that it is a most likely fault set conditioned on the set of soft outcomes m.

Assume that there exists a fault set x' (that is a 1-chain in G_T) such that $\mathbb{P}(x'|m) > \mathbb{P}(x|m)$. Consider the extension $\tilde{x}' = x' + x'_{\mathrm{soft}}$ as a 1-chain of $\tilde{G}_T$ obtained by adding the soft flip of x'. The value of x'_{soft} can be derived from x' and $\hat{s}$. By Lemma 4.2, the support of $\tilde{x}'$ contains a set of edge-disjoint paths in G_T connecting each vertex of $\hat{s}$ either with another vertex of $\hat{s}$ or with a boundary vertex. One can prove the existence of these paths by induction. If our set of paths contains two paths connecting to the boundary, we merge these two paths into a single paths in $\tilde{G}_T$. Then, each path of this set corresponds to an edge in $K(\hat{s})$ and the complete set of paths induces a perfect matching M' in $K(\hat{s})$. Moreover, the weight of the matching M', which is a sum of weights of edges included in $\tilde{x}'$, satisfies $w(M') \leq \sum_{e \in \tilde{x}} w(e)$. Based on Lemma 4.3, this weight is equal to

$$w(M') \leq \sum_{e \in \tilde{x}'} w(e) = C - \log \mathbb{P}(x'|m) \cdot$$

Using the assumption $\mathbb{P}(x'|m) > \mathbb{P}(x_M|m)$, this yields

$$\begin{aligned} w(M') &\leq C - \log \mathbb{P}(x'|m) \\ &< C - \log \mathbb{P}(x_M|m) \\ &< \sum_{e \in x_M} w_K(e) = w(M), \end{aligned}$$

which contradicts the minimality of M. This concludes the proof of the proposition. □

In the proof of Theorem 4.1 we relied on the following two lemmas.

Lemma 4.2. *Let x be a fault set for the graphical model (G_T, p, f, π) and let m be a set of soft outcomes observed in the measurement vertices. Then, the syndrome of x satisfies*

$$\hat{s}(m) = \partial_{V_\bullet}(\tilde{x}) \tag{9}$$

where $\tilde{x} = x + x_{\mathrm{soft}}$ and x_{soft} is the 1-chain of soft flips.

Proof. To prove that the syndrome is equal to $\partial_{V_\bullet}(\tilde{x})$, consider the syndrome value at a measurement vertex (a, t). Assume first that no soft flip occurs in this vertex. Then, the hard outcome and the ideal outcome are identical and by definition of the syndrome, we have $\hat{s}(a, t) = \overline{m}(a, t) + \overline{m}(a, t-1) \pmod 2 \cdot$ Using the definition of the ideal outcome, we see that this number is the parity of the number of edges of x that are incident to (a, t). This proves Eq. (9) in the absence of soft flip. This equation is also satisfied if a soft flip occurs in (a, t) thanks to the additional vertical soft edge incident to (a, t). □

Lemma 4.3. *Let x be a fault set for a graphical model (G_T, p, f, π) and let m be the set of soft outcomes measured. The probability $\mathbb{P}(x|m)$ of the fault set x conditioned on the soft measurement outcome m is given by*

$$\log \mathbb{P}(x|m) = C + \sum_{e \in \tilde{x}} w(e) \tag{10}$$

where $\tilde{x} = x + x_{\mathrm{soft}}$ and x_{soft} is the 1-chain of soft flips, for some constant C that is independent of x.

Proof. To compute $\mathbb{P}(x|m)$, we apply Bayes theorem to obtain

$$\mathbb{P}(x|m) \propto \mathbb{P}(m|x)\mathbb{P}(x)\cdot \tag{11}$$

Here, we abuse notation and use $\mathbb{P}(m|x)$ to represent the probability density function of the continuous random variable m conditioned on x. For simplicity, we focus on continuous distributions over sets of soft outcomes m, but the same argument applies to discrete soft outcome distributions.

We will consider the two terms of the right hand side of Eq. (11) separately.

Based on Eq. (4), we have $\mathbb{P}(x) = C_1 \prod_{e\in x} \frac{p_e}{1-p_e}$ where C_1 is the product of all the terms $(1-p_e)$ with $e \in E_T$. Taking the log, this yields

$$\log \mathbb{P}(x) = C_1' + \sum_{e\in x} + \log\left(\frac{p_e}{1-p_e}\right), \tag{12}$$

for some constant C_1'.

Consider now $\mathbb{P}(m|x)$. By definition of m, we have $\mathbb{P}(m|x) = \mathbb{P}(m|\overline{m})$. Because the soft outcomes in different measurement vertices (a,t) are independent, we have

$$\begin{aligned}
\mathbb{P}(m|\overline{m}) &= \prod_{(a,t)\in V_\bullet} f_{a,t}^{(\overline{m}_{a,t})}(m_{a,t}) \\
&= \prod_{\substack{(a,t)\in V_\bullet \\ \overline{m}_{a,t}=\hat{m}_{a,t}}} f_{a,t}^{(\hat{m}_{a,t})}(m_{a,t}) \\
&\times \prod_{\substack{(a,t)\in V_\bullet \\ \overline{m}_{a,t}\neq\hat{m}_{a,t}}} f_{a,t}^{(\hat{m}_{a,t}+1)}(m_{a,t}) \\
&= \prod_{(a,t)\in V_\bullet} f_{a,t}^{(\hat{m}_{a,t})}(m_{a,t}) \\
&\times \prod_{\substack{(a,t)\in V_\bullet \\ \overline{m}_{a,t}\neq\hat{m}_{a,t}}} \frac{f_{a,t}^{(\hat{m}_{a,t}+1)}(m_{a,t})}{f_{a,t}^{(\hat{m}_{a,t})}(m_{a,t})} \\
&= C_2 \prod_{\substack{(a,t)\in V_\bullet \\ \overline{m}_{a,t}\neq\hat{m}_{a,t}}} L_{a,t}(m_{a,t})
\end{aligned}$$

$C_2 = \prod_{(a,t)\in V_\bullet} f_{a,t}^{(\hat{m}_{a,t})}(m_{a,t})$ depends only on the set of soft outcomes m, since $\hat{m}$ is fully determined by m. The condition $\overline{m}_{a,t} \neq \hat{m}_{a,t}$ in the second product is equivalent to the presence of a soft flip in (a,t). Therefore, taking the log we obtain

$$\log \mathbb{P}(m|\overline{m}) = C_2' + \sum_{e\in x_{\text{soft}}} - \log L_{a,t}(m_{a,t})\cdot \tag{13}$$

By definition of the edge weights in the decoding graph, combining Eqs. (11) to (13) concludes the proof of the lemma. □

From Theorem 4.5 and Lemma 4.3 we can infer the following useful corollary.

Corollary 4.4. *For any graphical model satisfying (C1) and (C2), the soft MWPM decoder (Algorithm 1) successfully corrects all fault sets such that* $|\tilde{x}|_w < d_w/2$.

Proof. Let x be the fault set which occurs and let m be the set of soft outcomes observed. Assume that $|\tilde{x}|_w < d_w/2$. By Theorem 4.5, the soft MWPM decoder returns a fault set y such that $\mathbb{P}(y|m) \leq \mathbb{P}(x|m)$. By Lemma 4.3, this translates into

$$\sum_{e\in\tilde{y}} w(e) \leq \sum_{e\in\tilde{x}} w(e) \tag{14}$$

which means $|\tilde{y}|_w \leq |\tilde{x}|_w$. As a result, the residual fault set after correction $\tilde{x}+\tilde{y}$ has weight at most $|\tilde{x}+\tilde{y}| \leq 2|\tilde{x}|_w < d_w$ proving the decoder succeeds. □

4.3 Success of the soft UF decoder

Above we saw in Corollary 4.4 that the soft MWPM decoder successfully corrects all fault sets such that $|\tilde{x}|_w < d_w/2$. Here we establish a similar sufficient condition for the soft UF decoder.

Theorem 4.5. *For any graphical model satisfying (C1), (C2) and (C3), the soft UF decoder (Algorithm 2) successfully corrects any fault set such that* $|\tilde{x}|_w < d_w/2$.

Proof. Let x be a fault set such that $|\tilde{x}|_w < d_w/2$. Consider the graph $\tilde{H}_T(\gamma)$ represented in Figure 7 induced by the grown edges at the end of the growth. For each edge $e = \{u,v\}$ of $\tilde{H}_T$ where v is the splitting vertex, if $\gamma(e) = w(e)$, then $\tilde{H}_T(\gamma)$ contains the edge e, otherwise it contains an edge $\{u,u'\}$ with length $\gamma(e)$ which represents the grown part of the edge e.

Denote by $\Gamma_1, \Gamma_2, \ldots$ the growth rates in step 6 of Algorithm 2. The connected components $C_1, C_2, \ldots$ of $\tilde{H}_T(\gamma)$ satisfy

$$\sum_i \text{diam}_w(C_i) \leq 2\sum_j \Gamma_j, \tag{15}$$

$$\sum_{e\in\tilde{x}} \gamma(e) \geq \sum_j \Gamma_j. \tag{16}$$

The first equation holds because during the jth growth step, the selected cluster grows in all directions of Γ_j. Moreover, because the growing cluster is odd, this growth step covers at least a fraction Γ_j of an edge of x, leading to the second equation. Combining the two equations above, we obtain

$$\sum_i \mathrm{diam}_w(C_i) \leq 2 \sum_{e \in \tilde{x}} \gamma(e) \cdot \tag{17}$$

Let $\tilde{y}$ be the fault set returned by the peeling decoder in step 9 and let $\tilde{z} = \tilde{x} + \tilde{y}$. Denote by $\tilde{z}_1, \tilde{z}_2, \ldots$ the connected components of $\tilde{z}$. By construction $\tilde{y}$ is included in $\tilde{H}_T(\gamma)$. The only edges of $\tilde{z}$ outside of $\tilde{H}_T(\gamma)$ are the edges of $\tilde{x}$ such that $\gamma(e) = 0$. As a result, we have

$$\sum_k \mathrm{diam}_w(z_k) \leq \sum_i \mathrm{diam}_w(C_i) + \sum_{\substack{e \in \tilde{x} \\ \gamma(e)=0}} w(e) \tag{18}$$

$$\leq 2 \sum_{e \in \tilde{x}} \gamma(e) + \sum_{\substack{e \in \tilde{x} \\ \gamma(e)=0}} w(e) \tag{19}$$

$$\leq 2|\tilde{x}|_w < d_w. \tag{20}$$

Therein, the second inequality is obtained by applying Eq. (17). Because the last round of measurement is assumed to be perfect and the decoder returns a fault set $\tilde{y}$ which has the same syndrome as $\tilde{x}$, the residual fault set after correction $\tilde{z}$ has trivial syndrome and we proved that it obeys $|\tilde{z}| < d_w$. Therefore, applying (C3), the decoder succeeds. □

5 Performance of soft decoders

In this section we analyze the performance of some of the decoders defined in Section 3 under the soft noise models defined in Section 2. In particular we compare the soft Union Find decoder that we have introduced with the standard hard Union Find decoder that has access only to the hardened outcomes produced by discretizing the soft measurement outcomes. In Section 5.1 we first specify the protocol we use to evaluate the error correction performance, along with other definitions used in the numerical analysis. Then in Section 5.2 and Section 5.3 we present our numerical results for the performance of the soft Union Find decoder under soft phenomenological and soft circuit noise respectively.

5.1 Error correction protocol

It can be desirable to define a notion of *logical error rate* as the probability that a logical operation fails given a specific noise model and decoding scheme. In this section we describe how we estimate the logical error rate of a noise model equipped with a decoder using Monte Carlo simulations. Our simulations use a protocol starting with a perfectly prepared code state which undergoes T rounds of noisy syndrome measurements before a final round of perfect syndrome measurement, which specifies a graphical noise model (G_T, p, f, π).

In a Monte Carlo run of this protocol, first a fault set x is sampled according to the distribution $\mathbb{P}$ associated with the noise model. For each fault e in x, the corresponding residual error π_e is applied to the data qubits. Then, for each measurement vertex (a, t) (including the final round of perfect measurement), the ideal outcome $\overline{m}_{a,t}$ is computed and a soft outcome $m_{a,t}$ is sampled according to the distribution $f_{a,t}^{(\overline{m}_{a,t})}$. Based on the set of soft outcomes, the decoder returns a fault set y and a correction

$$\pi(y) = \prod_{e \in y} \pi_e \tag{21}$$

is applied to the data qubits intending to cancel the effect of x. The residual error on the data qubits after correction is then $\pi(x) + \pi(y)$.

Since the protocol ends with a perfect round of measurement, the decoders studied here are guaranteed to produce a correction with a residual error which is either a stabilizer or a non-trivial logical operator for the surface code. We say the decoder *succeeds* if the residual error $\pi(x) + \pi(y)$ is a stabilizer. Otherwise, we say the decoder *fails*. With a distance-d surface code, the failure probability of the protocol $p_d^{\mathrm{fail}}(T)$ is the expected value that the protocol fails, and in practice we estimate it from the fraction of failures among a finite number of samples. The decoders we study act separately on X and Z errors. We often find it convenient to separately consider the probability $p_d^{X\mathrm{fail}}(T)$ of a logical X failure of the protocol, irrespective of whether or not there is a logical Z failure.

There are a number of approaches in the literature to estimate a logical error rate from the failure probability of this kind of protocol. The simplest and most standard approach is to simply set $T = d$ and take $p_d^{\mathrm{fail}}(d)$ itself to be an estimate of the logical error rate. The reason for setting $T = d$ in this approach is that typically logical error operations (such as lattice surgery) with the surface code are assumed to take d rounds to ensure fault tolerance. However, the fact that the protocol ends with a perfect measure-

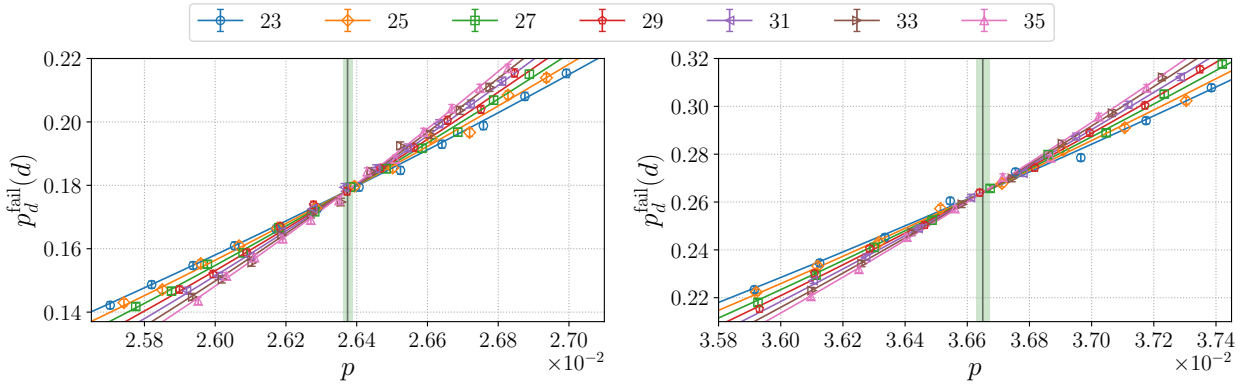


Figure 8: The failure probability of the protocol for d rounds of error correction with soft phenomenological noise using the hard Union Find decoder (left) and the soft Union Find decoder (right). In this noise model the X and Z errors are identical and independent, with the X error probability $p_D = p$, no hard ideal outcome flips $p_M = 0$, and with Gaussian soft noise with a spread σ selected such that $p_{M,\text{hardened}} = p$. The threshold value p^* for each decoder is estimated from the crossings of curves of different distance, and one standard deviation of uncertainty is shaded.

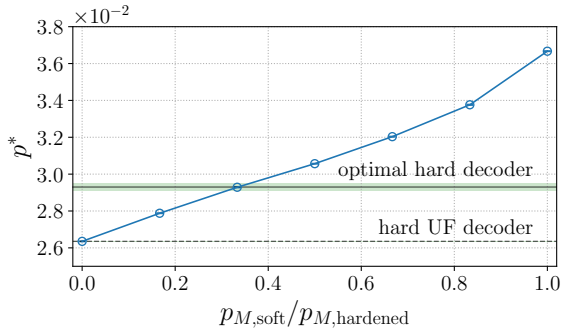


Figure 9: The threshold p^* obtained with the soft decoder with soft phenomenological noise with different ratios of soft to hard noise in the measurement. In this noise model the X and Z errors are identical and independent, with the X error probability $p_D = p$, with a variable ratio $r = p_{M,\text{soft}}/p_{M,\text{hardened}}$ but with the overall hardened flip probability $p_{M,\text{hardened}} = p$. The threshold of the hard Union Find decoder is the same for all values of r and is indicated with a dashed line. Note that $r = 1$ corresponds to the setting of Figure 8 in which there is no hard measurement flip, while $r = 0$ corresponds to the only measurement noise being a hard flip. The optimal threshold with a hard decoder was estimated in Ref. [21] and is indicated with a solid horizontal line with numerical uncertainty indicated with green shading.

ment round can lead this approach to significantly underestimate the true logical failure rate of a logical operation which takes d rounds [18]. Another drawback of this approach is that some logical operations may not take d rounds.

Here we instead estimate the logical failure rate per round, which we denote by $\bar{p}_d$, which can then be multiplied by the number of rounds in a logical operation to indicate its logical error rate. To avoid dependence on the perfect preparation and final stabilizer measurement round in the protocol on our estimate, we use a model of the protocol which applies for long times T. Our model is based on the assumption that during each round a logical X error occurs with probability $\bar{p}/2$ independently of other rounds [39]. After T rounds, there is a logical X failure in this model if an odd number of rounds have experienced logical X errors, which occurs with probability

$$\hat{p}^{X\ \text{fail}}(T) = \frac{1-(1-\bar{p})^T}{2}, \tag{22}$$

which can be inverted to give $\bar{p} = 1-(1-2\hat{p}^{X\ \text{fail}}(T))^{1/T}$. We use a hat to differentiate the failure probability $\hat{p}^{X\ \text{fail}}(T)$ of our model from the failure probability $p^{X\ \text{fail}}(T)$ of the protocol itself. Assuming the validity of this model becomes accurate for large T, we take the logical failure rate per round $\bar{p}_d$ to be calculated from the protocol's failure probability according to

$$\bar{p}_d(T) = 1-(1-2p_d^{X\ \text{fail}}(T))^{1/T}, \tag{23}$$

$$\bar{p}_d = \lim_{T\to\infty}\left(\bar{p}_d(T)\right). \tag{24}$$

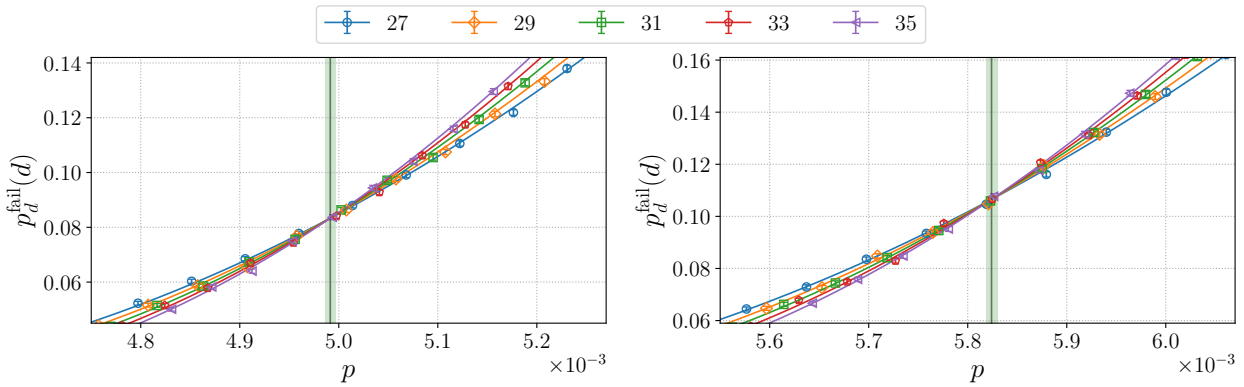


Figure 10: The failure probability of the protocol for d rounds of error correction with soft circuit noise using the hard Union Find decoder (left) and the soft Union Find decoder (right). We set p_{IG}, p_{IM} and p_{CNOT} equal to p, set $p_M = 0$ and use $f^{(0)} = \mathcal{N}(+1, \sigma^2)$ and $f^{(1)} = \mathcal{N}(-1, \sigma^2)$ with σ chosen such that $p_{M,\text{hardened}} = 10p$. The threshold value p^* for each decoder is estimated from the crossings of curves of different distance, and one standard deviation of uncertainty is shaded.

In practice we estimate $\bar{p}_d$ by evaluating $\bar{p}_d(T)$ for a large value of T. More details on this model's validity, and on the numerical convergence of Eq. (24) can be found in Appendix C.

The *error correction threshold* is the value of a single-parameter noise model below which error correction can be performed to achieve arbitrarily good protection by increasing the code distance. For noise models which have a number of parameters such as the soft noise models we have introduced, the concept of a threshold generalizes to a threshold surface [40]. Alternatively, one can introduce constraints on the parameters of a nosie model so that only one free parameter remains, and then consider the threshold value of the resulting single-parameter noise model. There are many approaches to numerically estimate the value of the threshold, all of which can be expected to agree in the limit of large code distances [41] because they are asymptotic properties of a phase boundary [4]. Here we estimate the threshold p^* of single-parameter noise model using the standard approach of identifying the intersections of the curves $p^{\text{fail}}(d)$ for different distances as a function of the parameter p.

5.2 Performance under soft phenomenological noise

Here we consider the soft phenomenological noise model which was defined in Section 2.3 and use the notation therein. In this model, the X and Z errors are generated and corrected independently. For simplicity we focus on the X errors here – the Z errors are handled in the same way.

Recall that in this model, probabilities p_D and p_M are assigned to horizontal and vertical edges in the X-type fault graph G_T respectively, and the pair of Gaussian probability density functions $f^{(0)} = \mathcal{N}(+1, \sigma^2)$ and $f^{(1)} = \mathcal{N}(-1, \sigma^2)$ are assigned to each measurement vertex in G_T.

In Figure 8 we obtain a single-parameter noise model from the phenomenological noise model by setting $p_D = p$, $p_M = 0$ and setting σ such that $p_{M,\text{hardened}} = p$, where $p_{M,\text{hardened}}$ is calculated according to Eq. (3). We plot the failure probability of the protocol for d rounds using the soft UF decoder and the hard UF decoder, and estimate the threshold p^* by considering the crossings of the resulting curves for different values of d. Note that the failure probabilities $p_d^{\text{fail}}(T)$ reported include failures of both X and Z type. We observe that the soft UF decoder significantly outperforms the hard UF decoder, exhibiting a threshold of $3.665(2) \times 10^{-2}$ versus $2.637(1) \times 10^{-2}$. Moreover, the optimal threshold of a decoder using hard information only is $2.93(2) \times 10^{-2}$ [21] which is still below the value obtained using the soft UF decoder.

In Figure 9 we repeat this analysis again with $p_D = p$ and $p_{M,\text{hardened}} = p$, but with different fixed values of $r = p_{M,\text{soft}}/p_{M,\text{hardened}}$. For each value of r, this specifies a single-parameter noise model for which we can estimate the threshold using the same approach as was used in Figure 8 for the case $r = 1$. We plot these estimated threshold values for various values of r in Figure 9.

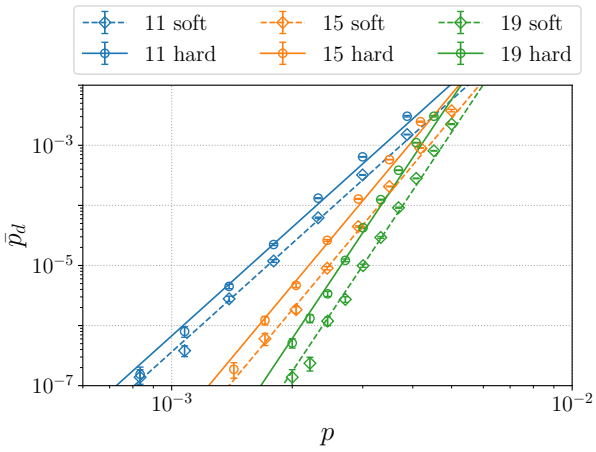


Figure 11: The failure probability per round for low error rates with the same soft circuit noise parameterization as in Figure 10. We estimate the failure rate per round $\bar{p}_d$ from the failure probability of the protocol for $T = 1000$ rounds using Eq. (24).

Note that by construction the hard noise models which are obtained by hardening the soft phenomenological noise models we study in Figure 8 and Figure 9 reduce to the standard single-parameter phenomenological noise model. In particular, the hardened version of the soft noise model for all values of r has X error on each qubit with probability $p_D = p$ and outcome flips of each plaquette measurement with the same probability $p_{M,\text{hardened}} = p$.

5.3 Performance under soft circuit noise

Here we consider the soft circuit noise model which was defined in Section 2.4. Recall that in this model, probabilities p_{IG}, p_{IM} and p_{CNOT} specify the probabilities of each possible fault of idle qubits during CNOT time steps, idle qubits during measurement time steps, and faults of CNOT operations. Additionally, the probability p_M specifies the flip of ideal outcomes, and probability distribution functions $\{f^{(0)}(\mu), f^{(1)}(\mu)\}$ characterize the soft noise. For the numerical studies here we use the standard exclusive circuit noise model to generate the faults (see Appendix B), while we use the inclusive circuit noise model is Section 2.4 to specify the edge weights of the decoder as described in Section 3.2. To improve the performance of the decoder, we merge all edges sharing the same endpoints in the decoding graph and combine their edge weights using the formula given in Appendix E of [18].

In Figure 10 we obtain a single-parameter noise model from the soft circuit noise model by setting $p_{IG} = p$, $p_{IM} = p$, $p_{\text{CNOT}} = p$, $p_M = 0$ and setting $f^{(0)} = \mathcal{N}(+1, \sigma^2)$ and $f^{(1)} = \mathcal{N}(-1, \sigma^2)$ with σ chosen such that $p_{M,\text{hardened}} = 10p$. We plot the failure probability of the protocol for d rounds using the soft UF decoder and the hard UF decoder, and estimate the threshold value of p by considering the crossings of the resulting curves for different values of d. We observe that the soft UF decoder outperforms the hard UF decoder, exhibiting a threshold of $5.824(6) \times 10^{-3}$ versus $4.991(5) \times 10^{-3}$. In Figure 11 we estimate the failure rate per round $\bar{p}_d$ using the soft UF decoder and the hard UF decoder with Eq. (24) for $T = 1000$ rounds.

For many hardware approaches, the readout fidelity can be significantly lower than the gate fidelity, which motivated us to consider a measurement flip probability $p_{M,\text{hardened}}$ which was ten times larger than the gate error probability in Figure 10. In Table 1 we list a number of threshold values including those for soft circuit noise but with $p_{M,\text{hardened}}$ equal to the gate error probability, in which case the threshold gap for the hard and soft decoder is less pronounced due to the relatively larger effects of ancilla qubit errors during the syndrome extraction circuit.

soft noise	soft UF threshold	hard UF threshold
phenomenological	3.665(2) %	2.637(1) %
circuit $p_{M,\text{hardened}} = p$	0.727(1) %	0.702(1) %
circuit $p_{M,\text{hardened}} = 10p$	0.5824(6) %	0.4991(5) %

Table 1: Thresholds observed when using the soft and hard decoders for various soft noise models. For soft phenomenological noise we set $p_D = p$, $p_M = 0$ and σ is chosen such that $p_{M,\text{hardened}} = p$. We consider two cases for soft circuit noise, each with $p_{IG} = p_{IM} = p_{\text{CNOT}} = p$ and $p_M = 0$, but with different $p_{M,\text{hardened}}$.

6 Measurement time tradeoff

In this section, we establish that the use of soft information can provide an advantage in the overall logical cycle time of a quantum computing platform

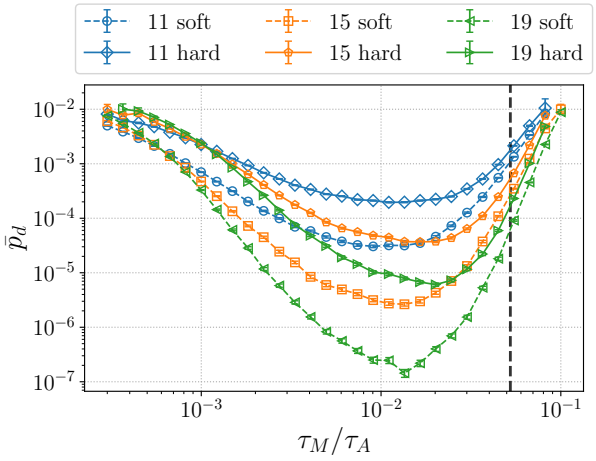


Figure 12: The logical error rate per round $\bar{p}_d$ for the parametric circuit noise model defined in section Section 6 as a function of measurement time τ_M. The τ_M which minimizes $\bar{p}_d$ depends on the distance and decoder. The vertical dashed line marks the measurement time that minimizes the average soft-flip probability of a single measurement with respect to measurement time (instead of the logical error rate), and leads to sub-optimal logical error rates.

in a model that considers the effects of measurement time. In real quantum error correction applications, selecting a measurement time for measurements represents a trade-off between measurement noise and data noise: Using too short a measurement time gives little information about the state of the ancilla. However, too long a measurement time gives time for additional errors to accumulate on the data.

We define an experimentally motivated variant of the soft circuit noise model where the noise parameter for each fault location is adjusted based on the duration that each circuit operation takes. Recall that in the soft circuit noise model, probabilities p_{IG}, p_{IM} and p_{CNOT} specify the probabilities of each possible fault of idle qubits during CNOT time steps, idle qubits during measurement time steps, and faults of CNOT operations. Additionally, p_M specifies the probability of a flip of an ideal outcome, and the probability distribution functions $\{f^{(0)}(\mu), f^{(1)}(\mu)\}$ characterize the soft noise. In our *parametric circuit noise model*, we consider:

- $p_{IG} = 1 - e^{-\frac{\tau_G}{\tau_D}}$,
- $p_{IM} = 1 - e^{-\frac{\tau_M}{\tau_D}}$,
- $p_{\text{CNOT}} = 1 - e^{-\frac{\tau_G}{\tau_D}}$,
- $p_M = 0$ and $f^{(\bar{\mu})}(\mu) = f^{(\bar{\mu})}(\mu; \tau_M, \tau_A, \tau_F)$.

This noise model assumes depolarizing noise, with additional Gaussian soft noise with amplitude damping during measurement. As such, our *parametric circuit noise model* is expressed in terms of the depolarizing time τ_D, the gate and measurement times τ_G and τ_M, along with additional parameters which specify the amplitude damping channel including the relaxation time τ_A and the fluctuation time τ_F as described in Section 1.4 and Appendix A. As in Section 5.3 we use the standard exclusive circuit noise model to generate the faults in our numerical simulations here, while we use the inclusive noise model to specify the edge weights of the decoder.

In Figure 12 we explore the effect of measurement time on the failure probability. In this plot, we set $\tau_G = 10\,\text{ns}$, $\tau_D = 30\,\mu\text{s}$, $\tau_A = 15\,\mu\text{s}$, $\tau_F = 100\,\text{ns}$ and vary τ_M. These parameters are within the range that can be expected to be achievable using near-term experiments [42–46]. We plot the failure rate per round $\bar{p}_d$ using the soft UF decoder and the hard UF decoder, by using Eq. (24) for $T = 1000$ rounds.

In contrast, we may choose τ_M to minimize the average soft flip probability $\frac{1}{2}\mathbb{P}(\text{soft flip}|0) + \frac{1}{2}\mathbb{P}(\text{soft flip}|1)$ for a single measurement under the Gaussian soft noise with amplitude damping model (a metric often considered in experimental demonstrations). This ignores the errors that accumulate in the data qubits during the measurement of the ancilla, but minimizes the probability of errors in the hard decision for each measurement (for details see Appendix A).

For a long measurement time τ_M, the data qubit noise rate per round is high and as a result the logical failure probability approaches that of a maximally mixed state. If the measurement time is too short, the information obtained by the syndrome extraction circuit is not reliable enough, which translates into a high logical error rate. In order to obtain the best possible logical qubit, we should select the measurement time that minimizes the logical error rate. In Figure 12, we observe that the optimal measurement time using the soft decoder is reached around $\tau_M/\tau_A = 1 \times 10^{-2}$ with a logical error rate per round close to 1×10^{-7} for distance 19. For comparison, if the measurement time is selected by minimizing the average soft-flip probability, the measurement time is roughly five times longer and, for distance 19, the logical error rate per round increases by nearly three

orders of magnitude to 1×10^{-4}. In these numerical results, we also observe that the optimal measurement time for the soft UF decoder is shorter than the optimal measurement for the hard UF decoder, which indicates that metric to optimize is not simply a function of the soft flip probabilities and the error rates on data qubits (as these are the same for the hard and soft decoders).

7 Conclusion

We have described a general framework that incorporates soft information into fault-tolerant quantum error correction with the surface code. This framework is independent of the physical realization of the qubits, and requires only knowledge of the distributions of soft outcomes conditioned on the qubit state. We give explicit constructions of two soft decoders for the surface code: a soft Minimum Weight Perfect Matching decoder (which we show identifies a most likely fault set for soft information), and a soft Union-Find decoder. Both of these decoders have the same computational complexity as their counterparts that handle only hard information, while the soft Union-Find decoder has lower computational overhead than the soft Minimum Weight Perfect Matching decoder.

We introduce two error models to evaluate the decoder performance: one where the syndrome is corrupted by Gaussian noise, and another where the syndrome is corrupted by Gaussian noise and amplitude damping. We show that under these error models the soft Union-Find decoder outperforms its hard counterpart both in terms of error threshold as well as sub-threshold logical error rate. Notably, the soft Union-Find decoder has a threshold that is 25% larger than the best possible hard decoder for the surface code, as estimated by statistical mechanics models. These error models were also used to study the trade-off between measurement time and logical error rate, where we found a strong dependence between these quantities, and showed that optimizing the measurement time with awareness of error correction can reduce the measurement time five-fold while decreasing the the logical error rate a thousand fold (even for relatively modest surface code distances). This highlights the benefits of jointly optimizing the physical layer and the error correction layer.

It would be valuable to develop theoretical methods to study the optimal decoding threshold for soft noise in the surface code—for example, by searching for a mapping to a generalized classical random-bond Ising model in which subsets of binary spins are be replaced by continuous variables.

Beyond surface codes, it would be interesting to explore these soft decoders with other codes such as color codes [47], other surface code variants [48] and some quantum Low-Density Parity-Check codes [49].

Given the gains observed with the use of soft information in the surface code, we expect that the addition of soft information to the quantum fault tolerance arsenal will shorten the time horizon for useful scalable quantum computers.

8 Acknowledgment

M.E.B, M.P.S, and N.D. thank David Poulin for his friendship, inspiration, and mentorship, as well as encouragement in the early stages of this work. C.A.P. acknowledges helpful discussions with Evan Zalys-Geller and Microsoft Quantum for support during his internship. C.A.P. is supported in part by Air Force Office of Scientific Research (AFOSR), FA9550-19-1-0360.

References

[1] P. Shor, Fault-tolerant quantum computation, in *Proceedings of 37th Conference on Foundations of Computer Science* (1996) pp. 56–65.

[2] A. Y. Kitaev, Fault-tolerant quantum computation by anyons, Annals of Physics **303**, 2–30 (2003).

[3] R. Raussendorf and J. Harrington, Fault-tolerant quantum computation with high threshold in two dimensions, Physical Review Letters **98**, 190504 (2007).

[4] E. Dennis, A. Kitaev, A. Landahl, and J. Preskill, Topological quantum memory, Journal of Mathematical Physics **43**, 4452–4505 (2002).

[5] A. G. Fowler, A. M. Stephens, and P. Groszkowski, High-threshold universal quantum computation on the surface code, Physical Review A **80**, 052312 (2009).

[6] S. Bravyi, M. Englbrecht, R. König, and N. Peard, Correcting coherent errors with surface codes, npj Quantum Information **4**, 1–6 (2018).

[7] J. Wang, T. Courtade, H. Shankar, and R. D. Wesel, Soft information for LDPC decoding in flash: Mutual-information optimized quantization, in *2011 IEEE Global Telecommunications Conference-GLOBECOM 2011* (IEEE, 2011) pp. 1–6.

[8] D. J. Costello and G. D. Forney, Channel coding: The road to channel capacity, Proceedings of the IEEE **95**, 1150–1177 (2007).

[9] D. Gottesman, A. Kitaev, and J. Preskill, Encoding a qubit in an oscillator, Physical Review A **64**, 012310 (2001).

[10] K. Fukui, A. Tomita, and A. Okamoto, Analog quantum error correction with encoding a qubit into an oscillator, Physical Review Letters **119**, 180507 (2017).

[11] C. Vuillot, H. Asasi, Y. Wang, L. P. Pryadko, and B. M. Terhal, Quantum error correction with the toric Gottesman-Kitaev-Preskill code, Phys. Rev. A **99**, 032344 (2019).

[12] K. Noh and C. Chamberland, Fault-tolerant bosonic quantum error correction with the surface–Gottesman-Kitaev-Preskill code, Physical Review A **101**, 012316 (2020).

[13] K. Noh, C. Chamberland, and F. G. Brandão, Low overhead fault-tolerant quantum error correction with the surface-GKP code, arXiv preprint arXiv:2103.06994 (2021).

[14] C. Chamberland, K. Noh, P. Arrangoiz-Arriola, E. T. Campbell, C. T. Hann, J. Iverson, H. Putterman, T. C. Bohdanowicz, S. T. Flammia, A. Keller, *et al.*, Building a fault-tolerant quantum computer using concatenated cat codes, arXiv preprint arXiv:2012.04108 (2020).

[15] N. Delfosse and N. H. Nickerson, Almost-linear time decoding algorithm for topological codes, arXiv preprint arXiv:1709.06218 (2017).

[16] H. Bombin and M. A. Martin-Delgado, Homological error correction: Classical and quantum codes, Journal of Mathematical Physics **48**, 052105 (2007).

[17] N. Delfosse, Decoding color codes by projection onto surface codes, Physical Review A **89**, 012317 (2014).

[18] R. Chao, M. E. Beverland, N. Delfosse, and J. Haah, Optimization of the surface code design for majorana-based qubits, Quantum **4**, 352 (2020).

[19] N. Delfosse, V. Londe, and M. Beverland, Toward a Union-Find decoder for quantum LDPC codes (2021), arXiv:2103.08049 [quant-ph] .

[20] M. B. Hastings and J. Haah, Dynamically generated logical qubits (2021), arXiv:2107.02194 [quant-ph] .

[21] C. Wang, J. Harrington, and J. Preskill, Confinement-Higgs transition in a disordered gauge theory and the accuracy threshold for quantum memory, Annals of Physics **303**, 31–58 (2003).

[22] C. Berge, *Graphs and hypergraphs* (North-Holland Pub. Co., 1973).

[23] A. G. Fowler, M. Mariantoni, J. M. Martinis, and A. N. Cleland, Surface codes: Towards practical large-scale quantum computation, Physical Review A **86**, 032324 (2012).

[24] D. Litinski, A game of surface codes: Large-scale quantum computing with lattice surgery, Quantum **3**, 128 (2019).

[25] A. Y. Kitaev, Fault-tolerant quantum computation by anyons, Annals of Physics **303**, 2–30 (2003).

[26] N. P. Breuckmann, C. Vuillot, E. Campbell, A. Krishna, and B. M. Terhal, Hyperbolic and semi-hyperbolic surface codes for quantum storage, Quantum Science and Technology **2**, 035007 (2017).

[27] J. Gambetta, W. A. Braff, A. Wallraff, S. M. Girvin, and R. J. Schoelkopf, Protocols for optimal readout of qubits using a continuous quantum nondemolition measurement, Phys. Rev. A **76**, 012325 (2007).

[28] M. Nielsen and I. Chuang, *Quantum Computation and Quantum Information: 10th Anniversary Edition* (Cambridge University Press, 2011).

[29] A. Blais, R.-S. Huang, A. Wallraff, S. M. Girvin, and R. J. Schoelkopf, Cavity quantum electrodynamics for superconducting electrical circuits: An architecture for quantum computation, Phys. Rev. A **69**, 062320 (2004).

[30] J. I. Colless, A. C. Mahoney, J. M. Hornibrook, A. C. Doherty, H. Lu, A. C. Gossard, and D. J. Reilly, Dispersive readout of a few-electron double quantum dot with fast rf gate sensors, Phys. Rev. Lett. **110**, 046805 (2013).

[31] Y. Tomita and K. M. Svore, Low-distance surface codes under realistic quantum noise, Physical Review A **90**, 062320 (2014).

[32] M. R. Garey and D. S. Johnson, *Computers and Intractability: A Guide to the Theory of NP-Completeness* (W. H. Freeman & Co., USA, 1979).

[33] J. Edmonds, Paths, trees, and flowers, Canadian Journal of mathematics **17**, 449–467 (1965).

[34] V. Kolmogorov, Blossom V: a new implementation of a minimum cost perfect matching algorithm, Mathematical Programming Computation **1**, 43–67 (2009).

[35] W. Cook and A. Rohe, Computing minimum-weight perfect matchings, INFORMS journal on computing **11**, 138–148 (1999).

[36] V. V. Vazirani, A theory of alternating paths and blossoms for proving correctness of the $O(\sqrt{VE})$ general graph maximum matching algorithm, Combinatorica **14**, 71–109 (1994).

[37] S. Huang, M. Newman, and K. R. Brown, Fault-tolerant weighted Union-Find decoding on the toric code, Phys. Rev. A **102**, 012419 (2020).

[38] N. Delfosse and G. Zémor, Linear-time maximum likelihood decoding of surface codes over the quantum erasure channel, Physical Review Research **2**, 033042 (2020).

[39] Z. Chen, K. J. Satzinger, J. Atalaya, A. N. Korotkov, A. Dunsworth, D. Sank, C. Quintana, M. McEwen, R. Barends, P. V. Klimov, S. Hong, C. Jones, A. Petukhov, D. Kafri, S. Demura, B. Burkett, C. Gidney, A. G. Fowler, H. Putterman, I. Aleiner, F. Arute, K. Arya, R. Babbush, J. C. Bardin, A. Bengtsson, A. Bourassa, M. Broughton, B. B. Buckley, D. A. Buell, N. Bushnell, B. Chiaro, R. Collins, W. Courtney, A. R. Derk, D. Eppens, C. Erickson, E. Farhi, B. Foxen, M. Giustina, J. A. Gross, M. P. Harrigan, S. D. Harrington, J. Hilton, A. Ho, T. Huang, W. J. Huggins, L. B. Ioffe, S. V. Isakov, E. Jeffrey, Z. Jiang, K. Kechedzhi, S. Kim, F. Kostritsa, D. Landhuis, P. Laptev, E. Lucero, O. Martin, J. R. McClean, T. McCourt, X. Mi, K. C. Miao, M. Mohseni, W. Mruczkiewicz, J. Mutus, O. Naaman, M. Neeley, C. Neill, M. Newman, M. Y. Niu, T. E. O'Brien, A. Opremcak, E. Ostby, B. Pató, N. Redd, P. Roushan, N. C. Rubin, V. Shvarts, D. Strain, M. Szalay, M. D. Trevithick, B. Villalonga, T. White, Z. J. Yao, P. Yeh, A. Zalcman, H. Neven, S. Boixo, V. Smelyanskiy, Y. Chen, A. Megrant, and J. Kelly, Exponential suppression of bit or phase flip errors with repetitive error correction (2021), arXiv:arXiv:2102.06132 [quant-ph] .

[40] K. M. Svore, D. P. Divincenzo, and B. M. Terhal, Noise threshold for a fault-tolerant two-dimensional lattice architecture, Quantum Info. Comput. **7**, 297–318 (2007).

[41] M. E. Beverland, A. Kubica, and K. M. Svore, Cost of universality: A comparative study of the overhead of state distillation and code switching with color codes, PRX Quantum **2**, 020341 (2021).

[42] F. Arute, K. Arya, R. Babbush, D. Bacon, J. C. Bardin, R. Barends, R. Biswas, S. Boixo, F. G. S. L. Brandao, D. A. Buell, B. Burkett, Y. Chen, Z. Chen, B. Chiaro, R. Collins, W. Courtney, A. Dunsworth, E. Farhi, B. Foxen, A. Fowler, C. Gidney, M. Giustina, R. Graff, K. Guerin, S. Habegger, M. P. Harrigan, M. J. Hartmann, A. Ho, M. Hoffmann, T. Huang, T. S. Humble, S. V. Isakov, E. Jeffrey, Z. Jiang, D. Kafri, K. Kechedzhi, J. Kelly, P. V. Klimov, S. Knysh, A. Korotkov, F. Kostritsa, D. Landhuis, M. Lindmark, E. Lucero, D. Lyakh, S. Mandrà, J. R. McClean, M. McEwen, A. Megrant, X. Mi, K. Michielsen, M. Mohseni, J. Mutus, O. Naaman, M. Neeley, C. Neill, M. Y. Niu, E. Ostby, A. Petukhov, J. C. Platt, C. Quintana, E. G. Rieffel, P. Roushan, N. C. Rubin, D. Sank, K. J. Satzinger, V. Smelyanskiy, K. J. Sung, M. D. Trevithick, A. Vainsencher, B. Villalonga, T. White, Z. J. Yao, P. Yeh, A. Zalcman, H. Neven, and J. M. Martinis, Quantum supremacy using a programmable superconducting processor, Nature **574**, 505–510 (2019).

[43] V. Negîrneac, H. Ali, N. Muthusubramanian, F. Battistel, R. Sagastizabal, M. S. Moreira,

J. F. Marques, W. J. Vlothuizen, M. Beekman, C. Zachariadis, N. Haider, A. Bruno, and L. DiCarlo, High-fidelity controlled-z gate with maximal intermediate leakage operating at the speed limit in a superconducting quantum processor, Phys. Rev. Lett. **126**, 220502 (2021).

[44] A. Crippa, R. Ezzouch, A. Aprá, A. Amisse, R. Laviéville, L. Hutin, B. Bertrand, M. Vinet, M. Urdampilleta, T. Meunier, M. Sanquer, X. Jehl, R. Maurand, and S. De Franceschi, Gate-reflectometry dispersive readout and coherent control of a spin qubit in silicon, Nature Communications **10**, 2776 (2019).

[45] P. Jurcevic, A. Javadi-Abhari, L. S. Bishop, I. Lauer, D. F. Bogorin, M. Brink, L. Capelluto, O. Günlük, T. Itoko, N. Kanazawa, A. Kandala, G. A. Keefe, K. Krsulich, W. Landers, E. P. Lewandowski, D. T. McClure, G. Nannicini, A. Narasgond, H. M. Nayfeh, E. Pritchett, M. B. Rothwell, S. Srinivasan, N. Sundaresan, C. Wang, K. X. Wei, C. J. Wood, J.-B. Yau, E. J. Zhang, O. E. Dial, J. M. Chow, and J. M. Gambetta, Demonstration of quantum volume 64 on a superconducting quantum computing system, Quantum Science and Technology **6**, 025020 (2021).

[46] X. Xue, M. Russ, N. Samkharadze, B. Undseth, A. Sammak, G. Scappucci, and L. M. K. Vandersypen, Computing with spin qubits at the surface code error threshold (2021), arXiv:2107.00628 [quant-ph] .

[47] H. Bombin and M. A. Martin-Delgado, Topological quantum distillation, Physical Review Letters **97**, 180501 (2006).

[48] J. P. B. Ataides, D. K. Tuckett, S. D. Bartlett, S. T. Flammia, and B. J. Brown, The xzzx surface code, Nature communications **12**, 1–12 (2021).

[49] N. Delfosse, V. Londe, and M. Beverland, Toward a union-find decoder for quantum ldpc codes, arXiv preprint arXiv:2103.08049 (2021).

[50] J. Gambetta, A. Blais, M. Boissonneault, A. A. Houck, D. I. Schuster, and S. M. Girvin, Quantum trajectory approach to circuit qed: Quantum jumps and the zeno effect, Phys. Rev. A **77**, 012112 (2008).

[51] C. Gidney, Decorrelated depolarization, `https://algassert.com/post/2001` (2020), accessed: 2021-07-26.

[52] A. Gelman, J. B. Carlin, H. S. Stern, D. B. Dunson, A. Vehtari, and D. B. Rubin, *Bayesian data analysis* (CRC press, 2013).

A Gaussian soft noise with amplitude damping

We consider one of the simple measurement models described in Ref. [27], namely, the measurement of a qubit with finite $|1\rangle$ lifetime τ_A and finite signal-to-noise ratio. This model was originally proposed to describe the dispersive measurement of superconducting qubits, but it applies to many other solid-state qubit implementations such as quantum dots. We present the toy model here in some detail for completeness.

In our toy model we assume the Hilbert space of the quantum system is spanned by two orthogonal states $|0\rangle$ and $|1\rangle$. Once the measurement is turned on at time $\tau = 0$, the (classical) continuous time output signal of the measurement apparatus is given by

$$\mathrm{d}S(\tau) = v\ R(\tau)\ \mathrm{d}\tau + \xi\ \mathrm{d}W(\tau) \tag{25}$$

where v is the signal amplitude, $R(\tau)$ is the measurement response, ξ is the noise amplitude, and $\mathrm{d}W(\tau)$ is the Wiener increment (a white Gaussian noise process with variance $\mathrm{d}\tau$ and zero mean).

We assume the state of the system collapses instantaneously into one of the basis states once measurement starts at $\tau = 0$, and that $R(\tau)$ depends on the state of the system instantaneously, such that $R(\tau) = 1$ if the system is in state $|0\rangle$, and $R(\tau) = -1$ if the system is in state $|1\rangle$.

The instantaneous response is important because the quantum system can spontaneously decay at any moment from the state $|1\rangle$ to the state $|0\rangle$ (but will remain in the $|0\rangle$ indefinitely). The decay time K is an exponentially distributed random variable with rate $1/\tau_A$. If we compute the probability that the system is still in state $|1\rangle$ at time τ, we find that $\mathbb{P}(|1\rangle\,;\tau) = e^{-\tau/\tau_A}$ as expected from the physics of spontaneous decay.

Throughout this appendix we will use capital letters to denote random variables, and lower case letters otherwise. The probability density function for a random variable H will be denoted by $f_H(h)$, while the corresponding cumulative density function will be denoted by $F_H(h)$, where $F_H(h) = \int_{-\infty}^{h} \mathrm{d}h'\ f_H(h') = \mathbb{P}(H < h)$. Following the convention in the main body of the text, superscripted random variables indicate conditioning on the quantum basis state, while conditioning on other random variables is indicated with the | symbol.

A.1 Soft-outcome distributions

In order to determine what was the outcome of the quantum measurement, we inspect the measurement signal and aim to classify the observed signal as corresponding to a $|0\rangle$ or a $|1\rangle$ outcome. One approach is to simply integrate the measurement signal for some measurement time τ_M [2]. The resulting scalar is given by the random variable

$$S = \int_0^{\tau_M} \mathrm{d}S(\tau), \tag{26}$$

and we are free to choose τ_M in order to improve performance (*i.e.*, our ability to distinguish between S when the state is $|0\rangle$ and when the state is $|1\rangle$). We note that each realization of S corresponds to the soft outcome μ.

Then, we have that

$$S = \int_0^{\tau_M} \mathrm{d}S(\tau), \tag{27}$$

$$= \underbrace{\int_0^{\tau_M} \mathrm{d}\tau\ v\ R(\tau)}_{P} + \underbrace{\int_0^{\tau_M} \mathrm{d}W(\tau)\ n}_{Q}. \tag{28}$$

It should be apparent that $Q \sim \mathcal{N}(0, \xi^2\ \tau_M)$ regardless of the qubit state, while the distribution for P requires some additional consideration conditioned on the initial state of the qubit.

If the initial state is $|0\rangle$, we have that $P_0 = v\ \tau_M$, so that $S_0 \sim \mathcal{N}(v\ \tau_M, \xi^2\ \tau_M)$.

If the initial state is $|1\rangle$, then the state can decay at some random time K. We have that

$$P_1|K = \begin{cases} -v(2K - \tau_M), & K < \tau_M \\ -v\tau_M, & K \geq \tau_M \end{cases} \tag{29}$$

and where K has an exponential distribution with mean $\frac{1}{\tau_A}$.

In order to compute the distribution for P_1, we first consider the case where $\tau_M \to \infty$, so that the output of the integral is a function of the random variable K, *i.e.*,

$$g(K) = v(\tau_M - 2K) \tag{30}$$

$$g^{-1}(P) = \frac{\tau_M}{2} - \frac{P}{2v} \tag{31}$$

so that

$$\frac{\mathrm{d}}{\mathrm{d}P} g^{-1} = -\frac{1}{2v} \tag{32}$$

[2] The signal may be post-processed in other ways [27, 50], but we focus on direct integration for simplicity.

and thus the distribution for $g(K)$ is

$$f_{g(K)}(p) = \frac{1}{2v} f_K\left(\frac{\tau_M}{2} - \frac{p}{2v}\right) \tag{33}$$

where f_K is the distribution for the decay time (an exponential distribution).

Now, $g(K)$ differs from P_1 because τ_M is finite, so we condition the transformation on the decay time. In particular,

$$f_{P_1|K<\tau_M}(p) = \frac{f_{g(K)}(p)}{F_K(\tau_M)}, \tag{34}$$

$$f_{P_1|K\geq\tau_M}(p) = \delta(p + v\tau_M), \tag{35}$$

and if we combine these we obtain

$$f_{P_1}(p) = \Theta(p + v\ \tau_M)\ \frac{1}{2v}\ f_K\left(\frac{\tau_M}{2} - \frac{p}{2v}\right) + \delta(p + v\ \tau_M)\ \left[1 - F_K(\tau_M)\right] \tag{36}$$

where δ is the Dirac function, and $\Theta(\tau)$ is the Heaviside step function.

When $\tau_M \ll \tau_A$, decay events are unlikely, and thus S_1 is approximately $\mathcal{N}(-v\ \tau_M, \xi^2\ \tau_M)$. When $\tau_M \gg \tau_A$, a decay is almost certain to happen during the measurement, and S_1 is approximately the sum of a $Q \sim \mathcal{N}(0, \xi^2\ \tau_M)$ and an a linear function of a exponential random variable with mean $\frac{1}{\tau_A}$.

We can obtain the probability density function for S_1 by convolving f_{P_1} with f_Q, resulting in

$$f_{S_1}(s) = \frac{e^{-\frac{\tau_M}{\tau_A} - \frac{(v\tau_M+s)^2}{2\xi^2\tau_M}}}{4\xi v\tau_A\sqrt{2\pi\tau_M}} \cdot \left\{ 4v\tau_A + e^{\frac{\left[\xi^2\tau_M + 2v\tau_A(v\tau_M+s)\right]^2}{8\xi^2v^2\tau_A^2\tau_M}} \xi\sqrt{2\pi\tau_M} \times \left[\mathrm{erf}\left(\frac{\xi^2\tau_M + 2v\tau_A(s+v\tau_M)}{2\xi v\tau_A\sqrt{2\tau_M}}\right) - \mathrm{erf}\left(\frac{\xi^2\tau_M + 2v\tau_A(s-v\tau_M)}{2\xi v\tau_A\sqrt{2\tau_M}}\right)\right]\right\}, \tag{37}$$

so that we have analytical expressions for the conditional distributions of the soft outcomes.

In the main text we use a slightly different convention for the soft outcomes, where the conditional means are ± 1 in the absence of decays. This can be achieved by a simple change of variables, so that

$$f^{(0)}(\mu) = v\ \tau_M\ f_{S_0}\left(v\ \tau_M\ \mu\right), \tag{38}$$

$$f^{(1)}(\mu) = v\ \tau_M\ f_{S_1}\left(v\ \tau_M\ \mu\right). \tag{39}$$

We can obtain a more convenient parameterization by defining *the fluctuation time* $\tau_F = \frac{\xi^2}{v^2}$, which allows us to write the conditional distributions in terms of the dimensionless ratios $\frac{\tau_M}{\tau_F}$ and $\frac{\tau_M}{\tau_A}$, resulting in

$$f^{(0)}(\mu; \tau_M, \tau_\mathrm{A}, \tau_F) = \sqrt{\frac{\tau_M}{2\pi\tau_F}} e^{-\frac{(\mu-1)^2\tau_M}{2\tau_F}} \tag{40}$$

$$f^{(1)}(\mu; \tau_M, \tau_\mathrm{A}, \tau_F) = \sqrt{\frac{\tau_M}{2\pi\tau_F}} e^{-\frac{(\mu+1)^2\tau_M}{2\tau_F} - \frac{\tau_M}{\tau_A}} - \frac{1}{4}\frac{\tau_M}{\tau_A} e^{\frac{\tau_M\tau_F}{8\tau_A^2} + \frac{1}{2}\frac{\tau_M}{\tau_A}(\mu-1)} \times \left\{ \mathrm{erf}\left[\sqrt{\frac{\tau_M\tau_F}{8\tau_A^2}} + (\mu-1)\sqrt{\frac{\tau_M}{2\tau_F}}\right] - \mathrm{erf}\left[\sqrt{\frac{\tau_M\tau_F}{8\tau_A^2}} + (\mu+1)\sqrt{\frac{\tau_M}{2\tau_F}}\right]\right\} \tag{41}$$

It is natural to take τ_A, τ_F to be fixed, and vary τ_M to optimize the measurement. The justification for this is that τ_A is set by qubit properties (materials, design, and fabrication), while τ_F is set by amplifier properties (noise temperature, compression point, etc.) and other device properties (maximum tolerable signal power on the qubit, coupling strength between qubit and measurement apparatus, etc.)—all of which are fixed in an experiment.

The rough intuition is that τ_A sets an upper limit to τ_M. As long as $\tau_M \ll \tau_\mathrm{A}$, increasing γ_M decreases the soft-flip error rate. As τ_M approaches and surpasses τ_A, decay events cause the soft-flip error rate to increase. Similarly, τ_F sets the lower limit on τ_M. If τ_M is comparable to τ_F, the soft measurement distributions are dominated by Gaussian noise. As $\frac{\tau_M}{\tau_F}$ increases above 1, the distributions become distinguishable, as the overlap decays exponentially with $\frac{\tau_M}{\tau_F}$ (for $\tau_M \ll \tau_\mathrm{A}$). A low soft flip error rate can be achieved if $\tau_F \ll \tau_M \ll \tau_A$.

A.2 Soft-flip probabilities

We can convert this to conditional probabilities of soft flips by integrating, which yields

$$\mathbb{P}(\text{soft flip}|0) = \frac{1}{2}\left[1 + \mathrm{erf}\left(\frac{\beta}{\sqrt{2}} - \sqrt{\frac{\tau_M}{2\tau_F}}\right)\right], \tag{42}$$

$$\mathbb{P}(\text{soft flip}|1) = \frac{1}{2} - \frac{1}{2}\text{erf}\left(\frac{\beta}{\sqrt{2}} - \sqrt{\frac{\tau_M}{2\tau_F}}\right) + \frac{1}{2}\exp\left[\beta\sqrt{\frac{\tau_M\tau_F}{4\tau_A^2}} + \frac{\tau_M\tau_F}{8\tau_A^2} - \frac{\tau_M}{2\tau_A}\right] \times \left\{\text{erf}\left[\frac{\beta}{\sqrt{2}} - \sqrt{\frac{\tau_M}{2\tau_F}} + \sqrt{\frac{\tau_M\tau_F}{8\tau_A^2}}\right] - \text{erf}\left[\frac{\beta}{\sqrt{2}} + \sqrt{\frac{\tau_M}{2\tau_F}} + \sqrt{\frac{\tau_M\tau_F}{8\tau_A^2}}\right]\right\} \quad (43)$$

where β is the decision boundary for the hard decisions based on soft outcomes. The maximum likelihood hardening map corresponds to a particular foice for β as a function of τ_M/τ_F and τ_M/τ_A. We vary β and τ_M to optimize hard measurement performance.

B Inclusive and exclusive circuit noise models

Here we discuss the distinction between two variations of the circuit noise model: an inclusive model in which all faults are independent, and an exclusive model in which some faults are mutually exclusive. In Section 2.4 we presented an inclusive circuit model. The standard model of circuit noise model is an exclusive model, in which each of the components of a circuit can fail in the following specific ways:

- Idle qubits waiting for CNOT gates: fail with probability $\tilde{p}_{IG}$. When a failure occurs, an element of the set $\{X, Y, Z\}$ is uniformly sampled and applied.
- Idle qubits waiting for measurements: fail with probability $\tilde{p}_{IM}$. When a failure occurs, an element of the set $\{X, Y, Z\}$ is uniformly sampled and applied.
- CNOT gates: fail with probability $\tilde{p}_{\text{CNOT}}$. When a failure occurs, an element of the set of 15 non-trivial weight-two Pauli operators is uniformly sampled and applied.

Here faults on different locations are applied independently of one another, although faults which occur on the same operation are exclusive. The measurement in the inclusive and exclusive models are treated identically. The standard exclusive circuit noise model shown here and the inclusive circuit noise model described in Section 2.4 exactly equivalent as proven in Appendix E of [18]. The equivalence comes with a map for the probabilities between the two models:

- $\tilde{p}_{IG} = p_{IG} + O(p_{IG}^2)$.
- $\tilde{p}_{IM} = p_{IM} + O(p_{IM}^2)$.
- $\tilde{p}_{\text{CNOT}} = p_{\text{CNOT}} + O(p_{\text{CNOT}}^2)$.

For low error rates the second order corrections (which can be calculated using the formulas specified in Ref. [51]) are small. For example, for fault probabilities of one percent and below, the corrections are at most 5×10^{-5}. We therefore neglect any corrections between the exclusive and inclusive circuit noise model throughout this work.

C Logical error rate per round

Here we discuss the model described in Section 5.1 that we use to extract an estimate of the logical error rate per round from the probability $p_d^{X\text{ fail}}(T)$ of a logical X failure of the error correction protocol with a distance-d code over T rounds. Our model is similar to that in Reference [39] and is based on the assumption that during each round a logical X error occurs with probability $\bar{p}/2$ independently of other rounds. After T rounds, there is a logical X failure in this model if an odd number of rounds have experienced logical X errors, which occurs with probability

$$\hat{p}^{X\text{ fail}}(T) = \frac{1 - (1-\bar{p})^T}{2}, \quad (44)$$

which is a repeat of Eq. (22) in the main text. We use hats to distinguish the model from the X failure of the protocol itself.

While the assumptions that define this model may not apply to the protocol itself, for a carefully selected value of $\bar{p}$ and for large T the formula $\hat{p}^{X\text{ fail}}(T)$ fits the data taken for the protocol $p_d^{X\text{ fail}}(T)$ very well; see Figure 13. The good fit can be understood from the fact that each of the decoders acts somewhat locally in the 3D decoding graph, and the matching of errors which are well separated in this graph occurs almost independently. In the regime of low logical error rate, this can be expected to lead to logical errors (which are sparse in this regime) which are also independent of one another.

The above model includes no explicit restriction on the correlation between logical X and logical Z failures. Let us explore the consequences of some additional assumptions. We can make the additional

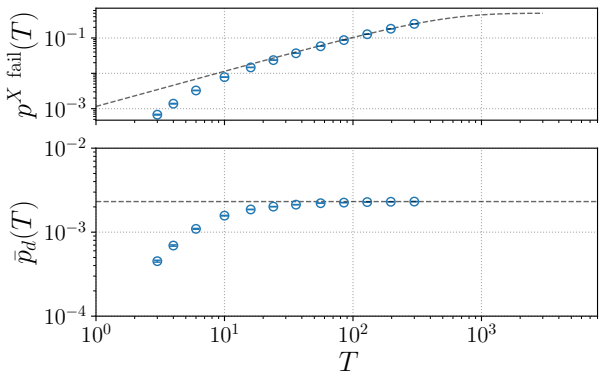


Figure 13: Convergence of $\bar{p}_d(T)$ calculated using Eq. (23) with T using the soft phenomenological noise model. (a) The protocol's X failure probability $p_d^{X\text{ fail}}(T)$ for a distance $d = 15$ surface code for a range of T. With a dashed line we show the model, namely $\hat{p}^{X\text{ fail}}(T) = (1-(1-\bar{p})^T)/2$ evaluated at $\bar{p} = \bar{p}_d(300)$. (b) For each data point $p_d^{X\text{ fail}}(T)$, we estimate $\bar{p}_d(T)$ according to Eq. (23). We observe a clear convergence of $\bar{p}_d(T)$ toward an asymptotic value by $T = 100$. We indicate $\bar{p}_d(300)$ by a dashed line.

assumption that during each round a logical Z error occurs with probability $\bar{p}/2$ independently of other rounds, such that $\hat{p}^{Z\text{ fail}}(T) = \hat{p}^{X\text{ fail}}(T)$. If furthermore we assume that X and Z failures are uncorrelated, then the overall probability $\hat{p}^{\text{fail,unc}}(T)$ of either a logical X failure, a logical Z failure or both is

$$\hat{p}^{X\text{ fail}}(T) + \hat{p}^{Z\text{ fail}}(T) - \hat{p}^{X\text{ fail}}(T)\hat{p}^{Z\text{ fail}}(T). \quad (45)$$

In this case of equal X and Z logical failure probabilities without correlation, $\bar{p}$ approximately corresponds to the overall failure probability of a single round $\hat{p}^{\text{fail,unc}}(1) = \bar{p} - \bar{p}^2/4$. As we are primarily interested in the regime of small $\bar{p}$, the $O(\bar{p}^2)$ term can be neglected, which justifies our reference to $\bar{p}$ as the logical failure probability per round.

D Simulation Methods

Here we describe some further details of the simulation methods we used to collect and analyze the data presented in the main text.

All of our data involves Monte Carlo sampling to estimate the probability q of success of the error correction protocol described in Section 5.1 given some noise model, code distance, and decoder. Given n trials of which k succeed, we use Bayesian inference to estimate the parameter of the corresponding Bernoulli distribution Bernoulli(q) [52]. We take the Jeffreys prior, so that the posterior distribution of q given the data is Beta($\frac{1}{2}+k, \frac{1}{2}+n-k$). We report the mean of the posterior distribution $\frac{k+1/2}{n+1/2}$ and 68% equal-tailed credible intervals calculated directly from the inverse cumulative distribution function of the Beta distribution. In many data points the intervals indicating statistical uncertainty (indicated by vertical lines with end caps) are smaller than the symbols which mark the data point.

For a noise model parameterized by a single parameter p, we often seek to identify a threshold value p^* of p such as in Figure 9 and Figure 11. We obtain a set of data points $p_d^{\text{fail}}(d)$ for a range of distances and values of p in the vicinity of the suspected value of p^*. Following the usual universal scaling ansatz for critical points in the study of phase transitions, we fit a quadratic in the scaled variable $x = (p-p^*)d^{1/\nu}$ to our data in this regime.

To minimize sensitivity to asymmetric measurement errors in models such as the amplitude damping model of Section 1.4, at each measurement round, each ancilla qubit is initialized in a known measurement eigenstate selected uniformly at random.